

Paul J. Wallace · Josef Dufek · Alfred T. Anderson ·
Youxue Zhang

Cooling rates of Plinian-fall and pyroclastic-flow deposits in the Bishop Tuff: inferences from water speciation in quartz-hosted glass inclusions

Received: 13 September 2001 / Accepted: 11 September 2002 / Published online: 1 November 2002
© Springer-Verlag 2002

Abstract Cooling rates inferred from water speciation in rhyolitic glass inclusions in quartz phenocrysts from the Bishop Tuff, California, vary over more than 5 orders of magnitude from about 10 to $<10^{-4}$ °C s⁻¹. Many of the cooling rates are within the previously published, experimentally calibrated range of this technique but the slowest rates ($<10^{-4}$ °C s⁻¹) are extrapolated. Such extrapolation suggests cooling rates as low as 10^{-8} °C s⁻¹ (0.3 °C year⁻¹) for the interiors of thick, pyroclastic-flow deposits. The temperatures at which OH and molecular H₂O species would be in equilibrium range from ~400 °C for glass inclusions from Plinian-fall deposits to ~250 °C for the most slowly cooled glassy inclusions from pyroclastic-flow deposits. Notwithstanding appreciable uncertainties, cooling rates correlate with depositional process (fall vs. flow deposition) and distance above the cold ground or below overlying, hot pyroclastic-flow deposits. Plinian inclusions within 2.5 m of the cold, pre-Bishop ground cooled at 1–10 °C s⁻¹, consistent with thermal modeling of small pumice clasts falling through cold air. Very slow, inferred cooling rates for pyroclastic-flow deposits ($\sim 10^{-6}$ to 10^{-8} °C s⁻¹) also

agree with thermal-conduction models. Faster cooling rates ($\sim 10^{-1}$ to 10^{-4} °C s⁻¹) for inclusions in the lowermost 0.5 m of pyroclastic-flow deposits reflect the effect of quenching against the cold ground. At Blind Spring Hill (east of Long Valley Caldera), intermediate cooling rates (10^{-3} to 10^{-6} °C s⁻¹) are observed in Plinian deposits overlain by, and partially interbedded with, pyroclastic-flow deposits, indicating that reheating of rapidly cooled Plinian inclusions can reset water speciation. Melt inclusions in pyroclastic-flow deposits are quenched to glass only if the deposit is relatively thin or has a relatively low emplacement temperature. In relatively thick or hot deposits, inclusions may be quenched to glass at the base of the deposit where it is more rapidly cooled by contact with the pre-eruption ground.

Keywords Cooling rate · Ignimbrite · Plinian eruption · Rhyolite · Volcanology · Water · Welded tuff

Editorial responsibility: T.H. Druitt

P.J. Wallace (✉)
Ocean Drilling Program, Texas A&M University, College Station,
TX 77845, USA
e-mail: pwallace@darkwing.uoregon.edu
Fax: +1-541-3464692

J. Dufek · A.T. Anderson
Department of the Geophysical Sciences, The University of Chicago,
Chicago, IL 60637, USA

Y. Zhang
Department of Geological Sciences, The University of Michigan,
Ann Arbor, MI 48109-1063, USA

Present address:

P.J. Wallace, Department of Geological Sciences,
University of Oregon, Eugene, OR 97403-1272, USA

Present address:

J. Dufek, Department of Geological Sciences,
University of Washington, Seattle, USA

Introduction

Cooling rates of pyroclastic material (Fig. 1) vary over many orders of magnitude. At one end of the spectrum, Plinian-fall tephra cool relatively rapidly as the particles move through air (Thomas and Sparks 1992; Tait et al. 1998; Hort and Gardner 2000; Xu and Zhang 2002). By contrast, tephra in pyroclastic flows cool very little during transport, resulting in relatively hot, pyroclastic-flow sheets that can become welded by compaction of volcanic ash and pumice (Smith 1960; Riehle 1973; Sparks et al. 1999). Between these two ends of the cooling-rate spectrum lie cooling rates that vary with distance from source, extent of cooling during transport, intercalation of fall and flow deposits, rate of accumulation, and final deposit thickness. Even Plinian-fall tephra cool at variable rates, depending on initial magma temperature, size of tephra clasts, and proximity to the vent, and under some circumstances fall deposits can become welded (e.g., Sparks and Wright 1979; Thomas and Sparks 1992).

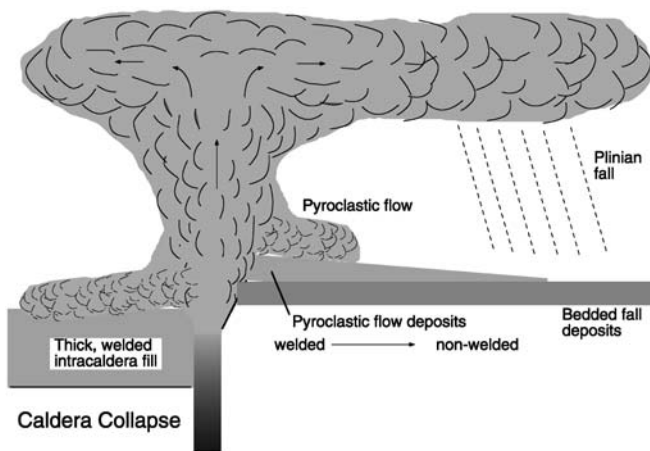


Fig. 1 Schematic illustration of depositional processes and facies in explosive volcanic eruptions. Cooling rates vary with mode of deposition (fall versus flow), distance from source, extent of cooling during transport, intercalation of fall and flow deposits, rate of accumulation, and final deposit thickness

Knowledge of cooling rates of tephra deposits is important for understanding eruption and post-depositional processes, such as welding, compaction, hydrothermal circulation, and alteration (e.g., Holt and Taylor 1998). Below we use measurements of water speciation in rhyolitic glass inclusions in quartz phenocrysts (Skirius 1990; Wallace et al. 1999; Anderson et al. 2000) and a recently published geospeedometer (Zhang et al. 2000) to infer cooling rates of some Plinian-fall and pyroclastic-flow deposits of the rhyolitic Bishop Tuff in California (Bailey et al. 1976). We also develop analytical and numerical heat-conduction models to help interpret the cooling-rate information derived from water-speciation data.

Samples and methods

The Bishop Tuff is a large-volume, rhyolitic tuff deposited during the 0.76-Ma eruption (van den Bogaard and Schirmick 1995) that formed Long Valley Caldera in eastern California (Fig. 2; Bailey et al. 1976). Quartz crystals, 0.15 to 3 mm in diameter, are the most abundant phenocryst mineral in most samples. Inclusions of rhyolitic melt (glass) are virtually ubiquitous in quartz phenocrysts in both Plinian and pyroclastic-flow Bishop Tuff (Fig. 3). Such inclusions are commonly 50 to 300 μm in diameter (Skirius 1990). The included glass varies from colorless (Fig. 3a, b) to tan (Fig. 3c) in Plinian deposits, and from slightly (Fig. 3e, k, l) to completely (Fig. 3j) devitrified in pyroclastic-flow deposits (Table 1). Rhyolitic glass inclusions from the Bishop Tuff have been analyzed for major, trace, and volatile elements in order to understand the origin and compositional evolution of rhyolitic magma in the Long Valley region (Anderson et al. 1989; Skirius 1990; Lu 1991; Dunbar and Hervig 1992; Wallace et al. 1999; Anderson et al. 2000).

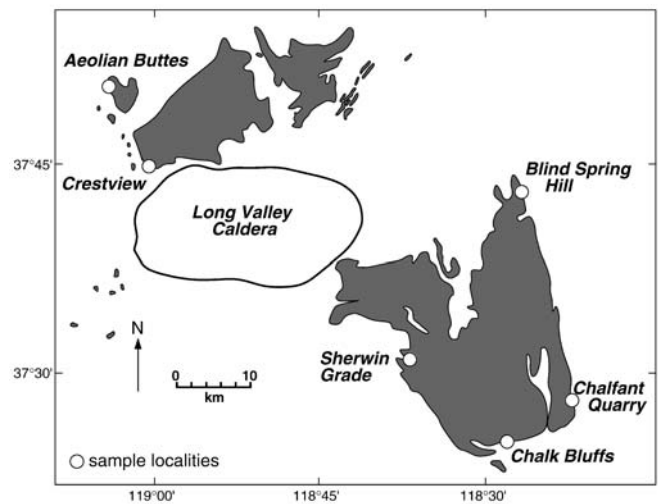


Fig. 2 Simplified map of the Bishop Tuff and Long Valley Caldera (based on Hildreth and Mahood 1986). Using locality numbers, vent distances, and stratigraphic units of Wilson and Hildreth (1997), the localities upon which this report is based are (1) Blind Spring Hill (locality 15, about 34 km E of the vent), where several quarries and adits expose about 5 m of Plinian-fall deposits overlain by more than 10 m of pyroclastic flows; (2) Chalfant Quarry (locality 21, about 42 km SE of the vent), a quarry exposing about 5 m of Plinian deposits including a pyroclastic flow that pinches out to the south and is approximately at the boundary between fall units 7 and 8; the Plinian-fall strata are overlain by >10 m of pyroclastic flow Ig2E; (3) Chalk Bluffs outcrop (near locality 57, about 38 km SE of the vent), 5 m of Plinian strata underlying >100 m of pyroclastic flow Ig2E; (4) Sherwin Grade roadcut (along Hwy. 395, ~1.5 miles ESE of Tom's Place, about 15 km SE of the vent), ~2 m of Plinian strata overlying Sherwin Till and overlain by ~10 m of Ig1Eb pyroclastic flow; (5) Crestview roadcut (near locality 208), 30+ m of pyroclastic flow lying on bouldery till and paleosol; and (6) Aeolian Buttes (near locality 104), about 5 m of Ig2NWb overlying granite

It is particularly important for this study that the previously analyzed glass inclusions are from pumices collected at known heights above or below cool or hot boundaries (such as the pre-eruption ground surface). Analyzed inclusions include those from both Plinian deposits and several, different pyroclastic-flow deposits with various initial temperatures and thicknesses (Fig. 2; Table 2). Thus, the samples allow us to compare inferred and modeled rates of cooling over a large range. We refer to certain Bishop pyroclastic-flow deposits by locality and, without individual attribution, by the stratigraphic designations of Wilson and Hildreth (1997) who use terms such as Ig2Ea to designate ignimbrite 2 found in the eastern (E) sector. The numbers and lowercase letters denote time-stratigraphic relations, such that Ig2 was emplaced after Ig1, and Ig2Eb was emplaced after Ig2Ea. We use the term pyroclastic-flow deposit to designate those deposits variously termed as welded tuff, ash-flow tuff, or ignimbrite.

Infrared spectroscopic studies show that water dissolved in rhyolitic glass occurs as two species: molecular H_2O and OH^- (Fig. 4; Newman et al. 1986; Silver et al. 1990). The relative abundance of the two species is

Table 1 Textures of Bishop melt (glass) inclusions. Textures are for uncracked inclusions >100 μm in diameter. Entries are for the dominant cases and would apply to more than about eight out of 10

Distance from pyroclastic-flow deposit base (up=+)	Blind Spring Hill quarries ^a ~5.2% H ₂ O ^b	Chalfant Quarry ^a ~5.6% H ₂ O	Crestview roadcut ^a ~4% H ₂ O	Aeolian Buttes ^a ~4% H ₂ O
~+3 m ^c	Opaque Devitrified			
~+1 m	Brown Bubbles Speckled	Tan/brown No bubbles Few <10 μm xls	Speckled Bubbles	Speckled ^d Bubbles Few <20 μm xls
~+0.3 m	Olive No bubbles	Tan – clear No bubbles	Clear No bubbles	Speckled Bubbles Few <20 μm xls
~-0.3 m	Tan No bubbles	Clear No bubbles		
~-1 m	Clear No bubbles	Clear No bubbles		

^a Locations of various sample sites are shown in Fig. 2

^b H₂O values are based on FTIR spectroscopic analyses as given in Table 2

^c Distances are approximate. The distances for the samples on which this table is based vary from one sample site to another by less than a factor of 2

^d The distance for the Aeolian Buttes samples is less than about 3 m, probably less than 1 m

dependent both on total water concentration (Zhang et al. 1997b, 2000) and on quench rate (Zhang et al. 1995, 1997a, 2000). The dependence on quench rate arises from the kinetics of the temperature-dependent reaction $\text{H}_2\text{O}_m + \text{O} = 2\text{OH}$, where H_2O_m is molecular H₂O, O is an anhydrous oxygen, and OH is a hydroxyl group (Zhang et al. 1995). Building on earlier studies at low total water concentration, Zhang et al. (2000) have recently calibrated the dependence of the speciation reaction on quench rate for glasses with up to 7.7 wt% total H₂O, and this includes the range encountered in the Bishop glass inclusions. Infrared spectroscopic data for all glass inclusions discussed in this paper are reported in Table 2. We use the algorithm of Zhang et al. (2000) to calculate cooling rates of our glass inclusions and thus their host pumice clasts from the Bishop Tuff.

Uncertainties in cooling rates depend on the quality of the IR spectra, uncertainties in inclusion thicknesses, and whether the quench rates and total H₂O contents fall within the range of experimental calibration of the geospeedometer. Most of the inclusions in Table 2 were analyzed using a Nicolet 60 SX Fourier transform infrared (FTIR) spectrometer with a microbeam sample compartment at the University of Chicago, using techniques described in Skirius (1990) and Wallace et al. (1999). In Table 2, we report only spectra of good quality for inclusions with the most accurate thickness measurements. For these inclusions, the uncertainty in intensity of each band (combined uncertainties from spectral noise, background fitting, and thickness) is about 2 to 4% relative. This results in an uncertainty in the cooling rate of a factor of 5 or better for inclusions within the experimental calibration range (10^{-4} to 10^2 °C s⁻¹). For inclusions that do not fall within the experimental cooling-rate calibration range, as is the case for most of our inclusions from pyroclastic-flow deposits, it is much

more difficult to estimate the uncertainty of extrapolation. The bigger the extrapolation, the less certain the cooling rate. A very rough estimate is that, at a cooling rate of 10^{-8} °C s⁻¹, the uncertainty in cooling rate would be about a factor of 50.

The above discussion is for doubly intersected inclusions with high-quality IR spectra. Calculated cooling rates based on analyses of inclusions that are partly or wholly enclosed within the quartz host are generally substantially less than those based on doubly intersected inclusions. This discrepancy reflects our tendency to overestimate the path length of the radiation through enclosed inclusions because of curvature of the inclusion-glass interface in the third dimension. The average path length through enclosed inclusions can be approximated by assuming an appropriate total H₂O concentration (based on stratigraphically equivalent, doubly intersected inclusions), and using that value to normalize the path length (estimated average inclusion thickness). Cooling rates observed for enclosed inclusions, after normalization of thicknesses, are similar to, but on average about a factor of 5 greater than, those observed for doubly intersected inclusions from fall unit 9 pumices in Chalfant Quarry. However, for speckled, partly devitrified inclusions from one pyroclastic-flow pumice clast, this normalization procedure yielded results nearly 2 orders of magnitude lower than doubly intersected inclusions from a subjacent sample. It is not clear if this specific discrepancy is due to the thickness normalization procedure or the partial devitrification of the inclusions. To avoid possible uncertainties related to the thickness normalization procedure, throughout the rest of this paper we only use data for glass inclusions that are doubly intersected.

The conceptual meaning of pyroclastic-flow deposit is that of a continuous, unsorted deposit, presumably the

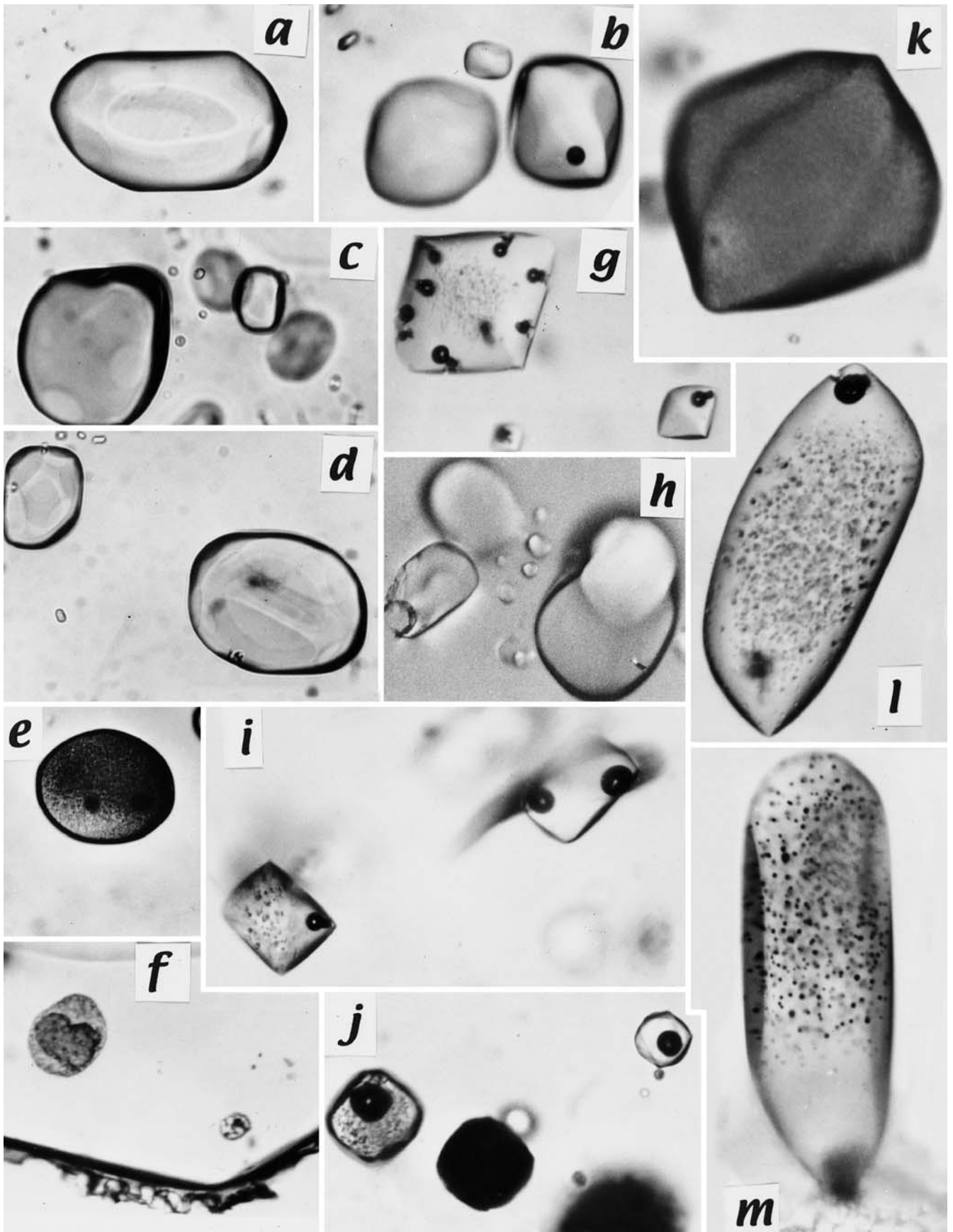


Fig. 3a–m Rhyolitic melt (glass) inclusions in phenocrysts vary in texture depending on cooling rate, composition (especially H₂O content), and host mineral. A sequence of progressively more slowly cooled inclusions from Skirius' Blind Spring Hill section is shown in **a–f**: with slower cooling, inclusions develop a darker color (**c**), bubbles (**b, e**) and more and larger crystals (**d–f**). Textures of other inclusions vary with H₂O content (**i, j, m**). The relation between cooling rate and the formation of bubbles and crystals varies: some rapidly cooled inclusions have bubbles without crystals (**b**), in some inclusions bubbles nucleated and grew on daughter crystals (**g, h, l**). Cracks allowed escape of H₂O and bubble formation in other inclusions (**i, j**), and a gradient in bubble density occurs in some hourglass inclusions (**m**). The quartz walls of some rapidly cooled inclusions are partly faceted (negative crystal shape, **a, c, d**), as also are some slowly cooled inclusions (**g, i, j**), and faceting is uncorrelated with cooling rate. Inclusions that cooled slowly at high temperature in densely welded ash flows are opaque and crystalline (**j**), as previously noted by Skirius et al. (1990). Slow cooling promotes the formation of crystals and bubbles in rhyolitic glass inclusions, but inclusion texture depends also on H₂O content and host mineral. Inclusions and host crystals are as follows. **a** Blind Spring Hill pumice clast BT87-5A-5-1, crystal 6 (F7, 4 m below the base of the main, overlying pyroclastic flow). The inclusion is 260 μm long, clear, colorless and bubble-free. **b** Same pumice clast as for **a**, quartz phenocryst 7. The bubble-bearing inclusion is ~155 μm long, and both inclusions are colorless and free of crystals. **c** Blind Spring Hill pumice clast BT87-13, crystal 15 (Ig1Eb, about 0.1 m above the base of the main pyroclastic flow). Inclusion is ~180 μm in diameter, light brown and free of bubbles and crystals. **d** Same pumice clast as in **c**, quartz phenocryst 19. The largest inclusion is ~210 μm long, has 10-μm-diameter daughter crystal(s) on the quartz wall, is colorless and partly faceted. **e** Blind Spring Hill pumice clast BT87-14-A1, quartz phenocryst 17 (Ig1Eb, 0.6–1.0 m above the base of the main ash flow). The inclusion is ~145 μm in diameter, finely speckled, brown and contains two bubbles; the easily visible one is ~10 μm in diameter and the other is ~20 μm in diameter. **f** Blind Spring Hill pumice clast BT87-15-B1, crystal 9 (Ig1Eb, 2–3 m above the base of the main ash flow). The inclusion is ~90 μm in diameter and its core is largely glassy, but most of the volume of the inclusion is microcrystalline. **g** Aeolian Buttes pumice clast LV81-18A-2B (less than a few meters above granitic basement underlying the Ig2NWb pyroclastic flow), crystal 118. The inclusion is ~100 μm in diameter, slightly speckled in its core, and has bubbles on pedestals of daughter crystals. **h** Chalfant pumice clast BC97-1-3a, crystal 5 (Ig1Eb). The big inclusion is ~210 μm long and contains a tiny daughter crystal (brightly birefringent – partly crossed polarizers) attached to its wall. **i** Aeolian Buttes pumice clast, same as **g**, quartz phenocryst 68 (Ig2NWb). The inclusion with two bubbles in the plane of a shadowy, glass-free crack is ~120 μm long, glassy and free of daughter crystals. **j** Variably devitrified inclusions in the same crystal from densely welded, vitrophyric ash flow near Aeolian Buttes (Ig2NWb). The small glassy inclusion in the *upper right* is ~40 μm in diameter and has a 10 vol% spherical (thus, above glass transition temperature) bubble reflecting loss of about 3 wt% H₂O from the melt, now glass. **k** Crestview pumice clast 327-2-1, crystal 26, inclusion 1 (3 m above the base of the pyroclastic flow Ig2NWa and its underlying paleosol). The inclusion is ~250 μm in diameter, dark brown, finely speckled and has a daughter crystal – *dark spot* lower left. Spectroscopic data for this inclusion are in Table 2. **l** Aeolian Buttes sample, same as **g**, crystal 10 (Ig2NWb). The inclusion is ~280 μm long, is coarsely speckled and has one bubble on a daughter crystal pedestal. **m** Crestview sample 327-3-18, crystal 2 (about 0.3 m above the base of the Ig2NWa pyroclastic flow). Hourglass inclusion is ~500 μm long, has no crystals or speckles but many tiny bubbles, and these fade out near its neck at the phenocryst rim (*bottom* of image)

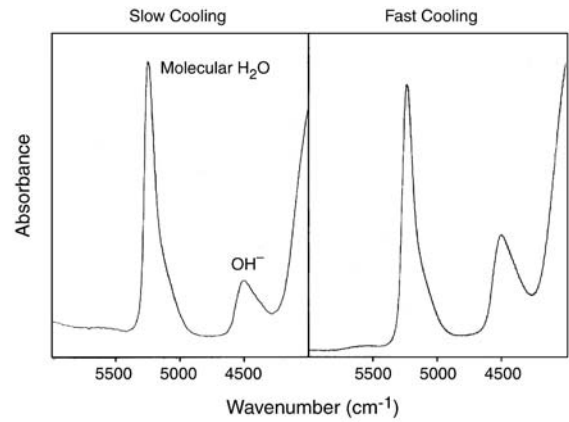


Fig. 4 Infrared spectra of hydrous, rhyolitic glass inclusions from the Bishop Tuff showing the greater H₂O_m/OH of slowly cooled inclusions. Absorbance on vertical axis is dimensionless (absorbance = $-\log I/I_0$, where I is intensity of light at a given wave number transmitted through the sample, and I_0 is intensity of incident light at the same wave number)

result of successive deposits (pyroclastic flows may show weak internal stratification) with little time between individual pulses. For simplicity, we sometimes use 'pyroclastic flow' or 'flow' instead of 'pyroclastic-flow deposit'. We do not intend to imply instantaneous formation of thick pyroclastic flows. Indeed, our studies may help constrain the rate at which thick pyroclastic-flow deposits form.

Results

Nominal cooling rates observed for Bishop glass inclusions range over more than 8 orders of magnitude from about 10 °C s⁻¹ to less than 10⁻⁸ °C s⁻¹ (Fig. 5), including almost the entire calibrated range (10² to 10⁻⁴ °C s⁻¹) and extrapolation to about 4 orders of magnitude slower. Glass inclusions from Plinian pumice typically cooled more rapidly than inclusions from pyroclastic-flow pumice, although there is considerable overlap between the two groups. The cause of this overlap is discussed below. Extrapolation suggests observed cooling rates as low as 10⁻⁸ °C s⁻¹ (0.3 °C year⁻¹) a few meters above the base of thick pyroclastic-flow deposits. The temperatures at which the measured water species would be in equilibrium range from ~450 °C for glass inclusions in Plinian-fall tephra to ~250 °C for the most slowly cooled inclusions from pyroclastic-flow pumice.

Though we recognize the potentially large uncertainty of extrapolating beyond the calibration range of the water-speciation cooling-rate speedometer, observed cooling rates correlate with depositional process (Plinian pumice-fall vs. pyroclastic-flow deposition) and distance above the cold ground or below overlying, hot pyroclastic flows. At Blind Spring Hill (east of Long Valley Caldera; Fig. 2), the uninterrupted, basal Plinian-fall deposit is about 4.5 m thick (Skirius 1990; Wilson and Hildreth

Table 2 Infrared spectroscopic data and calculated cooling rates for Bishop melt (glass) inclusions

Inclusion ^a	A _{5,230} (mm ⁻¹)	A _{4,520} (mm ⁻¹)	H ₂ O (wt%)	q (°C s ⁻¹)	Log q	T _{ae} (°C)
Blind Spring Hill (early Bishop Tuff)						
BT-87						
2-A6	0.811	0.291	4.8	2.7E-01	-0.6	370
2-1-4.1	0.875	0.301	5.1	6.9E-01	-0.2	372
2-1-4.4	0.923	0.325	5.4	6.8E+00	0.8	392
2-1-7.1	0.892	0.326	5.3	7.9E+00	0.9	398
2-2-1.1	0.896	0.325	5.3	7.3E+00	0.9	396
3A-5-1	0.864	0.291	5.0	2.1E-01	-0.7	362
3A-5-2	0.836	0.283	4.8	8.5E-02	-1.1	357
5B-G4-2	0.740	0.265	4.3	9.4E-03	-2.0	350
5D-E5	0.870	0.297	5.1	4.5E-01	-0.3	369
5D-Lu1-1	0.960	0.316	5.5	2.9E+00	0.5	378
5D-Lu2-1	0.893	0.339	5.4	2.4E+01	1.4	412
5D-Lu2-2	0.904	0.329	5.4	1.0E+01	1.0	400
5-H12-1(HG)	0.862	0.317	5.2	3.7E+00	0.6	392
5-H12-2(HG)	0.932	0.323	5.5	5.6E+00	0.8	389
6A-B3	0.821	0.287	4.8	1.5E-01	-0.8	364
6A-B7-1	0.872	0.322	5.2	6.0E+00	0.8	397
6A-B7-2	0.852	0.317	5.1	3.8E+00	0.6	394
6B-52-8	1.081	0.266	5.8	5.5E-03	-2.3	312
6B-52-7	1.158	0.261	6.0	2.7E-03	-2.6	300
6B-52-1	0.988	0.264	5.4	3.9E-03	-2.4	318
7A-B6-1	0.903	0.273	5.1	1.6E-02	-1.8	337
7A-B6-2	0.936	0.279	5.2	4.0E-02	-1.4	340
7A-B6-3	0.944	0.289	5.3	1.4E-01	-0.8	350
7B-Lu1-1	0.931	0.275	5.2	2.2E-02	-1.7	336
7B-Lu2-1	0.964	0.264	5.3	4.0E-03	-2.4	321
8A-L1-2	1.040	0.270	5.6	9.9E-03	-2.0	320
8B-G11-1	1.006	0.250	5.4	3.1E-04	-3.5	302
8B-G12-1	1.043	0.265	5.6	4.6E-03	-2.3	314
8B-G12-2	0.942	0.242	5.1	6.2E-05	-4.2	299
8B-H4	1.061	0.284	5.8	7.3E-02	-1.1	332
10-Lu-1	1.161	0.240	6.0	4.6E-05	-4.3	279
10LuB	1.199	0.233	6.1	8.0E-06	-5.1	268
11A-C3-1	1.094	0.230	5.6	3.1E-06	-5.5	273
11A-C3-2	1.054	0.217	5.4	5.8E-08	-7.2	262
11A-Lu-1	1.220	0.232	6.2	6.9E-06	-5.2	266
11A-Lu-2	1.168	0.232	5.9	5.6E-06	-5.3	269
11B-E1	1.065	0.225	5.5	7.1E-07	-6.1	270
11B-Lu-1	1.064	0.237	5.5	1.7E-05	-4.8	282
11B-Lu-2	1.096	0.239	5.7	3.2E-05	-4.5	282
13-E7-1	1.124	0.226	5.7	9.1E-07	-6.0	266
13-E7-2-1	1.168	0.240	6.0	4.1E-05	-4.4	277
13-E7-2-2	1.140	0.233	5.8	6.7E-06	-5.2	272
13-E7-3	1.026	0.230	5.3	2.9E-06	-5.5	278
13-E9	1.241	0.228	6.2	2.5E-06	-5.6	260
13-LU-1	1.149	0.209	5.8	2.1E-09	-8.7	246
16-Lu-1	1.096	0.229	5.6	2.4E-06	-5.6	272
Sherwin Grade – Hwy. 395 (early Bishop Tuff)						
21A-2-1	1.058	0.252	5.6	4.3E-04	-3.4	299
21A-8-1	1.018	0.225	5.3	6.8E-07	-6.2	273
21A-8-2	1.009	0.228	5.3	1.5E-06	-5.8	277
21A-C7-1	0.992	0.232	5.2	4.7E-06	-5.3	283
21A-C7-2	1.160	0.279	6.1	4.4E-02	-1.4	319
21A-C8-1	1.080	0.271	5.8	1.2E-02	-1.9	317
21A-C11	1.001	0.248	5.3	2.2E-04	-3.7	300
21A-Lu2	0.966	0.246	5.2	1.4E-04	-3.8	301
Chalfant pumice quarry (middle Bishop Tuff)						
CHAL 1-2-1						
1.2.1	1.064	0.237	5.5	1.7E-05	-4.8	282
1.3.1	1.134	0.243	5.9	7.0E-05	-4.2	283
3.1.1	1.115	0.239	5.8	3.3E-05	-4.5	281
3.1.3	1.166	0.255	6.1	9.8E-04	-3.0	294
3.2.1	1.109	0.239	5.7	3.2E-05	-4.5	281
3.2.2	1.122	0.261	5.9	2.4E-03	-2.6	303

Table 2 (continued)

Inclusion ^a	A _{5,230} (mm ⁻¹)	A _{4,520} (mm ⁻¹)	H ₂ O (wt%)	q (°C s ⁻¹)	Log q	T _{ae} (°C)
CHAL 1-2-7						
1.1	1.103	0.218	5.6	7.2E-08	-7.1	259
HG 2.1	1.218	0.229	6.2	3.6E-06	-5.4	264
3.1	1.105	0.245	5.7	1.1E-04	-4.0	287
3.2	1.056	0.248	5.6	1.8E-04	-3.7	294
4.1	1.090	0.244	5.7	8.5E-05	-4.1	288
CHAL 20-35-1						
2.1	1.086	0.222	5.6	2.6E-07	-6.6	265
3.1	1.107	0.231	5.7	4.2E-06	-5.4	273
3.2	1.097	0.206	5.5	4.8E-10	-9.3	247
CHAL 20-35-4						
1.1	1.154	0.221	5.8	2.2E-07	-6.7	259
3.1	1.032	0.220	5.3	1.4E-07	-6.8	267
5.1	1.103	0.237	5.7	1.7E-05	-4.8	279
6.1	1.114	0.242	5.8	5.4E-05	-4.3	283
7.1	1.102	0.235	5.7	1.2E-05	-4.9	278
9.1	1.088	0.240	5.6	3.6E-05	-4.4	284
CHAL-9						
1.1	1.113	0.244	5.8	8.5E-05	-4.1	286
4.1	1.117	0.236	5.8	1.6E-05	-4.8	278
6.1	1.090	0.241	5.7	4.6E-05	-4.3	285
8.1	1.049	0.218	5.4	7.3E-08	-7.1	263
BC97-1-3a						
4-2	1.037	0.224	5.4	4.7E-07	-6.3	270
13-1	1.038	0.248	5.5	1.8E-04	-3.7	296
8-1	1.271	0.243	6.4	1.3E-04	-3.9	274
3-1	0.857	0.206	4.5	1.5E-09	-8.8	266
3-2	0.771	0.248	4.4	3.9E-04	-3.4	325
7-1	1.021	0.214	5.2	1.6E-08	-7.8	261
Chalk Bluffs (middle Bishop Tuff)						
CBF-17						
5.1	1.077	0.217	5.5	5.6E-08	-7.3	260
6.1	1.096	0.204	5.5	1.5E-10	-9.8	244
7.1	1.011	0.198	5.1	1.0E-11	-11.0	245
8.1	1.141	0.220	5.8	1.8E-07	-6.8	259
CBF-18						
1.1	1.102	0.235	5.7	1.1E-05	-4.9	277
1.2	1.124	0.241	5.8	5.1E-05	-4.3	282
2.1	1.107	0.234	5.7	9.1E-06	-5.0	276
3.1	1.093	0.242	5.7	5.3E-05	-4.3	285
6.1	1.140	0.236	5.9	1.6E-05	-4.8	276
Crestview (late Bishop Tuff)						
327-3/91 ^b						
1.1.1	0.653	0.243	3.9	4.7E-04	-3.3	338
1.1.2	0.591	0.304	4.0	4.1E+00	0.6	428
1.2	0.714	0.305	4.5	2.1E+00	0.3	403
5.1	0.830	0.224	4.5	1.1E-06	-6.0	290
5.2	0.681	0.298	4.3	1.1E+00	0.0	400
7.1	0.680	0.310	4.4	4.0E+00	0.6	416
8.1	0.668	0.268	4.1	2.9E-02	-1.5	366
8.2	0.697	0.332	4.6	2.6E+01	1.4	439
8.3	0.436	0.228	2.9	7.5E-04	-3.1	366
327-3-1 ^c						
1.1	0.705	0.244	4.1	3.3E-04	-3.5	330
2.1	0.745	0.248	4.3	5.3E-04	-3.3	329
2.3	0.772	0.263	4.5	5.7E-03	-2.2	342
4.1	0.745	0.249	4.3	6.0E-04	-3.2	330
4.2	0.700	0.229	4.0	1.2E-05	-4.9	312
8.1	0.721	0.280	4.4	1.0E-01	-1.0	371
9.1	0.728	0.236	4.1	5.1E-05	-4.3	317
12.1	0.661	0.230	3.8	2.7E-05	-4.6	320
13.1	0.741	0.240	4.2	1.0E-04	-4.0	320

Table 2 (continued)

Inclusion ^a	A _{5,230} (mm ⁻¹)	A _{4,520} (mm ⁻¹)	H ₂ O (wt%)	<i>q</i> (°C s ⁻¹)	Log <i>q</i>	T _{ae} (°C)
14.1	0.682	0.241	4.0	2.1E-04	-3.7	330
20.1	0.692	0.231	4.0	2.4E-05	-4.6	317
327-3-3 ^c						
14.1	0.752	0.254	4.3	1.5E-03	-2.8	335
18.1	0.691	0.242	4.0	2.2E-04	-3.6	329
327-3-5 ^c						
3.1	0.874	0.253	4.8	6.4E-04	-3.2	318
3.2	0.961	0.254	5.2	6.5E-04	-3.2	310
17.1	0.925	0.223	4.9	5.0E-07	-6.3	279
19.1	0.868	0.252	4.8	5.3E-04	-3.3	317
327-3-8 ^c						
26.1.1	0.659	0.215	3.7	5.8E-07	-6.2	302
327-2-1 ^d						
26.1	0.788	0.218	4.3	2.3E-07	-6.6	287
26.2	0.790	0.210	4.3	1.6E-08	-7.8	278
26.4	0.772	0.208	4.2	8.8E-09	-8.1	277
26.5	0.776	0.223	4.3	1.2E-06	-5.9	295
27.1	0.739	0.221	4.1	9.8E-07	-6.0	297
27.2	0.759	0.212	4.1	5.0E-08	-7.3	284
27.4	0.737	0.208	4.0	1.4E-08	-7.8	282
28.1	0.809	0.202	4.3	4.6E-10	-9.3	266
28.5	0.772	0.202	4.1	1.1E-09	-8.9	271
28.7	0.830	0.199	4.4	1.0E-10	-10.0	261
29.1	0.781	0.209	4.2	1.2E-08	-7.9	278
29.3	0.754	0.197	4.0	1.1E-10	-10.0	266

^a All inclusions except for those from BC97-1-3a were analyzed using a Nicolet 60 SX Fourier transform infrared (FTIR) spectrometer with a microbeam sample compartment at the University of Chicago, using techniques described in Skirius (1990) and Wallace et al. (1999). Inclusions in BC97-1-3a were analyzed at the University of Michigan. Absorbances are recalculated to a sample thickness of 1 mm. Concentrations of total dissolved H₂O were calculated using the calibration of Zhang et al. (1997b) and represent the sum of molecular H₂O (5,230 cm⁻¹) and OH⁻ (4,520 cm⁻¹). The calibration of Zhang et al. (1997b) is not precise at such high H₂O contents, but the absolute H₂O content is not critical for this study. Cooling rates (*q*) are calculated from Zhang et al. (2000) as described in the text. Apparent equilibrium temperatures (T_{ae}) are calculated using Eq. 8 of Ihinger et al. (1999). Inclusions labeled 'HG' are hourglass inclusions. Sample localities are shown in Fig. 2. Time-stratigraphic relations of all samples, except BC97-1-3a, in the detailed stratigraphic framework of Wilson and Hildreth (1997) are shown in Fig. 2 of Wallace et al. (1999). Sample BC97-1-3a is from a pyroclastic flow deposit (Ig1Eb) at Chalfant Quarry.

^b Collected from base of section

^c Collected from 30 cm above base

^d Collected from 3 m above base

1997) and is overlain by ~1 m of interbedded flow and pumice-fall deposits (Fig. 6). Above that is a pyroclastic-flow deposit (Ig1Eb) with a base at 5.7 m above the pre-eruptive ground surface. The pyroclastic-flow deposit above 5.7 m was probably originally ~15 m thick; a minimum of 9 m of pyroclastic-flow deposit is exposed in this section but the top of the flow is eroded and not exposed (Skirius 1990). An uneroded, stratigraphically equivalent pyroclastic flow exposed nearby (Wilson and Hildreth 1997, locality 95) is about 17 m in total thickness and overlain by later Plinian-fall deposits. Our sampled section (Wilson and Hildreth 1997, locality 15) was more protected from pyroclastic flows by the pre-eruption topography of Blind Spring Hill. Therefore, the original thickness of the pyroclastic-flow deposit was probably <17 m at our sampled section.

At our Blind Spring Hill section, Plinian inclusions within 2.5 m of the pre-Bishop ground cooled at 1 to 10 °C s⁻¹. The cooling rate of Plinian inclusions decreases upwards to about 10⁻³ °C s⁻¹ at 4 m (Fig. 6). At ~5 m height in the section, where fall and flow deposits are interbedded, the cooling rate is ~10⁻⁵ °C s⁻¹. Cooling rates are ~10⁻⁶ °C s⁻¹ at the base of the overlying pyroclastic flow (Fig. 6). A plausible explanation for the upward decrease in cooling rates observed for the Blind Spring Hill section is that all of the Plinian tephra cooled at rapid rates (1–10 °C s⁻¹) during fallout and were cold when deposited. Subsequently, hot pyroclastic flows formed the overlying deposit, causing reheating of the underlying Plinian deposit. Consistent with this explanation, the glass inclusions from the region in which pyroclastic flow and fall deposits are interbedded show cooling rates similar to the overlying pyroclastic-flow deposit but orders of

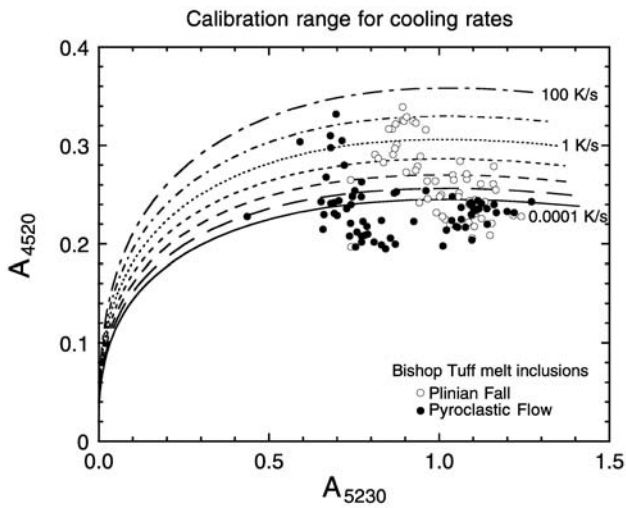


Fig. 5 Molecular H₂O absorbance (5,230 cm⁻¹) vs. OH absorbance (4,520 cm⁻¹). Absorbances are recalculated to a sample thickness of 1 mm. Lines of constant cooling rate are from Zhang et al. (2000); the range of cooling rate for which lines are shown corresponds approximately to the range of the experimental calibration data set. Data for Bishop Tuff glass inclusions are from Table 2. In this and subsequent figures, we have only used spectra of A quality as defined by Skirius (1990), because the noise in the poorer quality spectra results in large uncertainties in calculated cooling rates

magnitude slower than the basal Plinian deposits. Below we test this explanation further using our thermal modeling.

At the Chalfant quarry (Fig. 2), our data are mainly from Wallace et al. (1999), and focus on the uppermost Plinian-fall deposit (unit F9). Limited data on the overlying pyroclastic flow (Ig2Ea) and the Ig1Eb flow between F7 and F8 at Chalfant yield broadly similar, observed cooling rates (Fig. 7). The cooling rates of both Plinian-fall (F9) and pyroclastic-flow inclusions at Chalfant are around 10⁻⁶ °C s⁻¹, similar to those for inclusions in the Ig1Eb pyroclastic flow at Blind Spring Hill. Similar, slow cooling rates also characterize inclusions from pyroclastic-flow deposits at Chalk Bluffs (Figs. 2, 7). Slightly faster cooling rates (~10⁻⁴ °C s⁻¹) are observed for Plinian-fall pumice at the Sherwin Grade roadcut (Figs. 2, 7) where the fall deposits are only about 2 m thick and are overlain by many meters of pyroclastic flows. In all of these cases (Chalfant, Chalk Bluffs, Sherwin Grade), slowly cooled Plinian-fall inclusions are invariably within about 1.5 m of overlying pyroclastic flows. Plausibly the pyroclastic flows reheated the fall deposits and caused slow cooling.

We had hoped that, in pyroclastic-flow samples with only devitrified inclusions (presumably as a result of very slow cooling), we would be able to obtain cooling rates from reentrant glasses and hourglass inclusions (both remain glassy) and from rare, cracked glassy inclusions. However, at both Blind Spring Hill and Chalfant, such samples, taken from >1 m above the base of thick pyroclastic-flow deposits, yielded cooling rates that scatter very widely. This pattern needs more study but

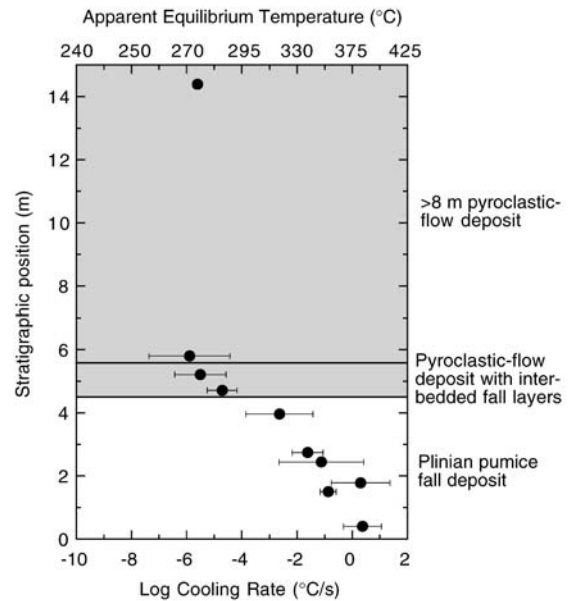


Fig. 6 Observed cooling rate versus stratigraphic position above base of deposit for glass inclusions from the Blind Spring Hill section (Fig. 2). Apparent equilibrium temperature shown along upper axis is the temperature at which the measured water speciation would be in equilibrium; note that the relationship between log cooling rate and T_{ae} is non-linear. Plotted points show the average (\pm standard deviation) of glass inclusions from a given stratigraphic horizon (commonly from a single pumice clast). Data are in Table 2. We have not shown data for inclusions that Skirius (1990) reports from clast BT87-6B and BT87-15. Inclusions from both these samples have highly anomalous cooling rates for their stated height. Inclusions reported from BT87-6B are green in color, in contrast to all other Plinian glass inclusions from this section, and similar inclusions do not, in fact, occur in the remaining clast fragment in the bag labeled 6B. Inclusions reported from BT87-15, which is from the overlying pyroclastic flow deposit, are clear glass whereas newly examined inclusions from this same stratigraphic level are devitrified. Accordingly, we use here only newly prepared inclusions from the clast fragments in bag 6B. The stratigraphic positions of Skirius' inclusions labeled 6B and 15 in her dissertation are uncertain

our tentative interpretation is that there are competing processes that affect OH/H₂O speciation in slowly cooled inclusions. Some possibilities are: (1) incipient devitrification includes the formation of hydrous minerals, providing another hydroxyl reservoir within the inclusion; (2) bubble-bearing, partially degassed inclusions (evidently cracked) have been affected by differential loss of molecular H₂O and OH⁻; (3) bubble-bearing inclusions have gained meteoric H₂O through cracks during cooling below the temperature at which speciation can re-equilibrate. Reliable cooling-rate observations seem mostly restricted to clear, glassy, uncracked inclusions.

Cooling rates decrease upwards above the base of the Mono lobe pyroclastic flow (Ig2NWa) at the Crestview roadcut near the NW margin of Long Valley Caldera (Fig. 2). This section exposes a >50 m thick, proximal pyroclastic-flow deposit (Hildreth, oral communication 1999). There is no underlying Plinian deposit at this locality. Glass inclusions from pumice collected from less

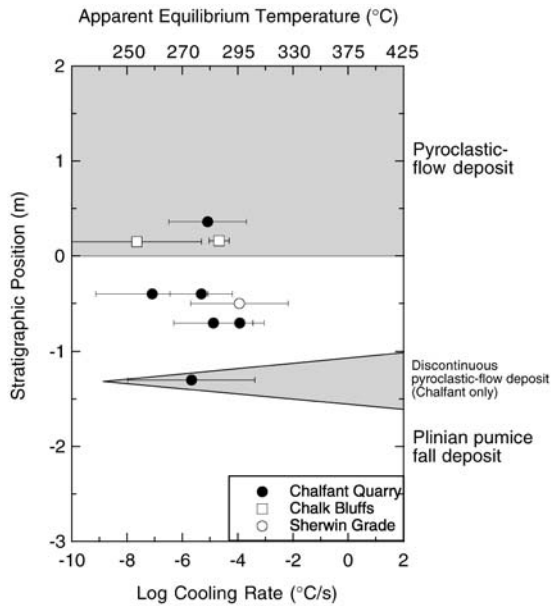


Fig. 7 Observed cooling rate versus stratigraphic position for glass inclusions from Chalfant Quarry, Chalk Bluffs, and the Sherwin Grade roadcut (Fig. 2). The contact between Plinian-fall pumice and overlying, thick pyroclastic-flow deposits is arbitrarily placed at 0 in order to compare the three sections. It is important to note, however, that this boundary is time-transgressive at the different localities (Wilson and Hildreth 1997). Note that at the Chalfant quarry, a thin, discontinuous lens of Ig1Eb is present between fall units F7 and F8. Data are in Table 2

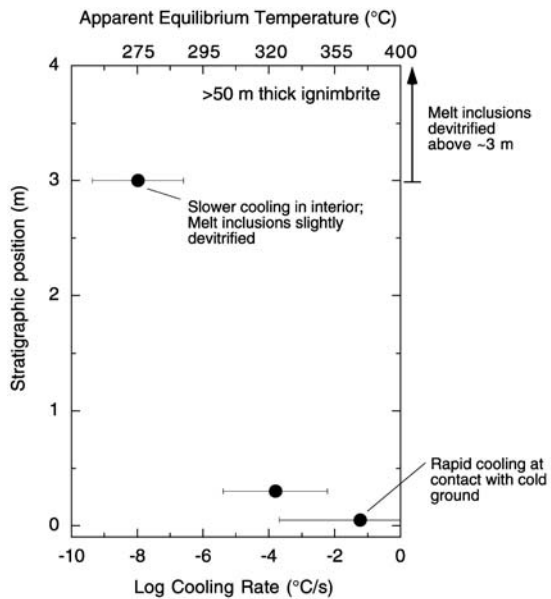


Fig. 8 Observed cooling rate versus stratigraphic position above base of deposit for glass inclusions from the Mono lobe pyroclastic flow (Ig2NWa) exposed at the Crestview roadcut (Fig. 2). Data are in Table 2

than 10 cm above the base of this section show cooling rates of $\sim 0.1 \text{ }^\circ\text{C s}^{-1}$ (Fig. 8). Samples collected 30 cm above base have significantly lower cooling rates of $\sim 10^{-4} \text{ }^\circ\text{C s}^{-1}$. By 3 m above base, the inferred cooling rate is $\sim 10^{-8} \text{ }^\circ\text{C s}^{-1}$. Most inclusions at this level have a speckled, slightly devitrified appearance (Fig. 31) and, in a clast from at least 5 m above the base, all uncracked glass inclusions are devitrified. The gradient in cooling rates in the Crestview section plausibly results from the quenching of a hot pyroclastic-flow deposit against the relatively cold, pre-eruption ground surface. Thermal modeling of this interpretation is developed below.

Discussion

We have shown above that an observed record of cooling conditions in Plinian-fall and pyroclastic-flow deposits can be obtained by analyzing H_2O_m and OH in rhyolitic glass inclusions. In the following sections, we compare our results for glass inclusions with theoretical cooling rates based on conductive-cooling models for Plinian-fall deposits (Tait et al. 1998) and for pyroclastic-flow deposits, as developed below. We then address the situation, quite common in the Bishop Tuff, in which pyroclastic-flow deposits overlie Plinian-fall material and appear to have reset the hydrous speciation in the Plinian glass inclusions. Finally, we discuss the conditions necessary for glass inclusions in pyroclastic-flow deposits to be quenched to glass instead of devitrifying under slow cooling conditions.

We developed a conductive-cooling model to compute theoretical rates of cooling that we could compare with our observations. The model, although simple, reveals a number of interesting and even counter-intuitive features when applied to cooling rates. We elaborate our model below and then apply it to our observations. To clarify the conceptual aspects of various cooling rates, we refer to cooling rates that we derive from spectroscopically determined $\text{H}_2\text{O}_m/\text{OH}$ as measured or observed cooling rates. We refer to experimentally imposed cooling rates as experimental. Cooling rates that we compute using our model of heat conduction we refer to as calculated or theoretical cooling rates.

Heat-conduction model

The interpretation of cooling rates inferred from hydrous speciation in glass inclusions is complicated by non-uniform cooling rates in natural deposits. Hydrous speciation records only a portion of the cooling history of a pyroclastic flow. The hydrous speciation in rhyolitic glass corresponds to a temperature (T_e) at which hydroxyl and molecular water would be in equilibrium (Zhang et al. 2000). Experimentally, a controlled constant rate of cooling will yield a final speciation, and this speciation will reflect both the cooling rate and a temperature of apparent equilibrium (T_{ae}). With faster cooling, final

speciations will correspond to higher values of T_{ae} . For constant rates of cooling and total water content, the T_{ae} and cooling rate are uniquely interdependent. During constant cooling the actual temperature at which the speciation no longer changes measurably is close to T_{ae} (Zhang et al. 2000). T_{ae} values calculated for Bishop glass inclusions are reported in Table 2.

In most natural, conductively cooling circumstances, the cooling rate is not constant but becomes slower at lower temperatures. If the natural cooling rate is approximately constant when T is close to T_{ae} , then the apparent, natural cooling rate is approximately the same as that implied by the experimentally controlled, constant cooling rate. However, it should be emphasized that the inferred, natural cooling rate strictly applies only to that part of the cooling history where T is close to T_{ae} .

Cooling rates in pyroclastic-flow deposits vary with height and time, and are governed by boundary conditions as well as flow thickness, emplacement temperature, and thermal diffusivity. The transfer of heat in pyroclastic-flow deposits with relatively large, horizontal extents is primarily by one-dimensional heat conduction:

$$\partial T / \partial t = \kappa \partial^2 T / \partial z^2, \quad (1)$$

where T is temperature, t is time, z is depth and κ is the thermal diffusivity (Carslaw and Jaeger 1959; Ryan et al. 1990; Reihle et al. 1995). The initial condition is difficult to specify. To be more generally applicable, we consider three different layers in our heat-conduction model (Fig. 9): layer 1 is a pyroclastic-flow deposit with

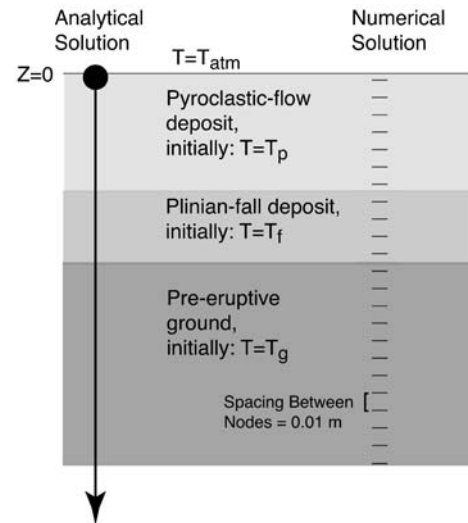


Fig. 9 Schematic representation of analytical and numerical, multi-layer heat-conduction models as described in the text. The *scale marker* to the left indicates that measurements are made from the top of the ash flow moving downwards. In the analytical solution the calculation domain extends to infinity and hence there is no bottom boundary. In the numerical finite-volume simulations the bottom boundary is extended sufficiently deep, so that the bottom nodes do not change their temperature appreciably as a result of conduction. The distance between the nodes in the finite-volume calculations was 0.01 m. Note that uniform initial temperatures are assigned to each of three layers: the pyroclastic-flow deposit, the Plinian-fall deposit, and the pre-eruptive ground

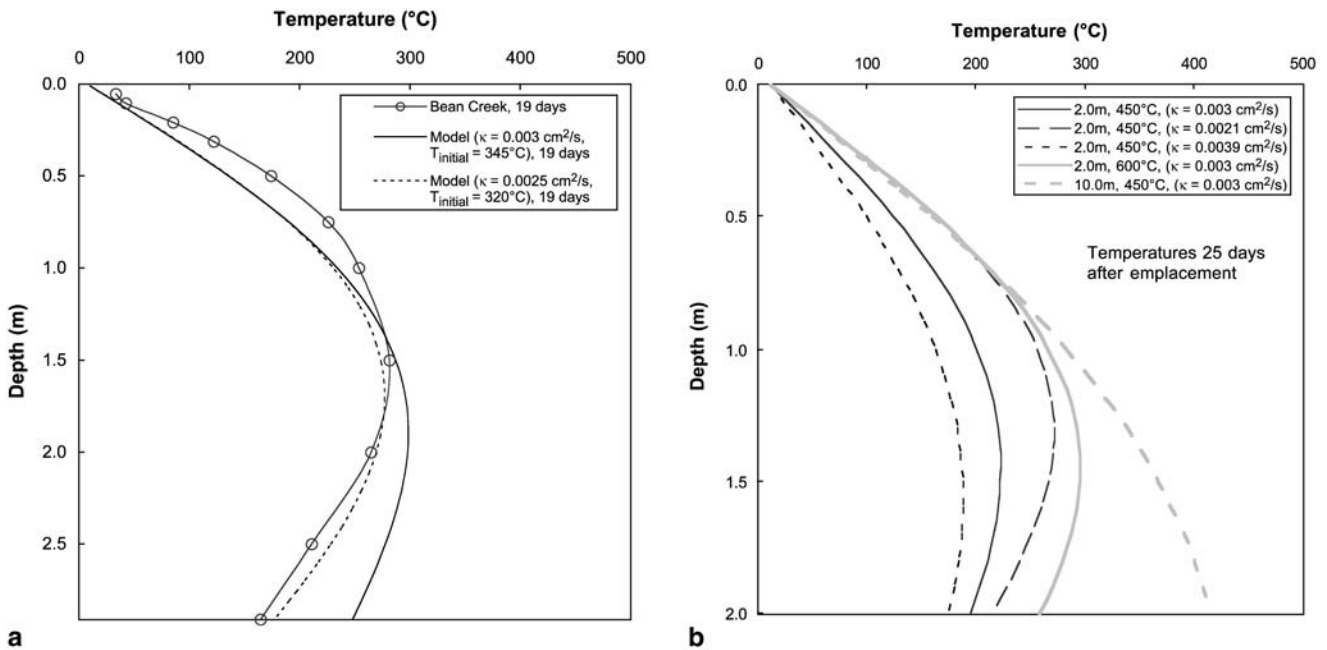


Fig. 10 a Comparison of observed and modeled temperature vs. depth for the Bean Creek pyroclastic-flow deposit, Mt. St. Helens. The curve compares the in-situ cooling profile observed 19 days after deposition (Ryan et al. 1990) to cooling profiles predicted by our model for an emplacement temperature of 320°C and a thermal

diffusivity of $0.0025 \text{ cm}^2 \text{ s}^{-1}$ (dashed line), and for an emplacement temperature of 345°C and a thermal diffusivity of $0.003 \text{ cm}^2 \text{ s}^{-1}$ (solid line). **b** Sensitivity of model calculations to variations in emplacement temperature, deposit thickness, and thermal diffusivity

temperature T_p , which is deposited on layer 2 (a Plinian-fall deposit with temperature T_f) which is deposited on layer 3 (the ground layer with temperature T_g). Hence, the initial condition is (Fig. 9):

$$T|_{t=0} = \begin{cases} T_p & 0 < z < z_1 \\ T_f & z_1 < z < z_2 \\ T_g & z > z_2 \end{cases} \quad (2)$$

Although the ground temperature should increase with depth, the typical depth scale in this study is no more than 100 m, leading to only negligible increases. Although our model is specific to three layers, the two-layer case can be easily accommodated (simply letting $z_2=z_1$). For more layers or other initial conditions, analytical solutions can be found using methods similar to those described below.

The depth below z_2 is assumed to be unlimited and, hence, no boundary condition is needed. The boundary condition at $z=0$ is assumed to be:

$$T|_{z=0} = T_{atm}, \quad (3)$$

where T_{atm} is the atmospheric temperature.

Given the above initial and boundary conditions, the heat-conduction problem can be solved as follows. The solution to the heat-conduction equation for a constant κ , a general initial condition of $\phi(z)$, and a zero boundary condition can be found in Carslaw and Jaeger (1959, section 2.4):

$$v(z, t) = \frac{1}{\sqrt{4\pi\kappa t}} \int_0^{\infty} \phi(z') \cdot \left[e^{-(z-z')^2/(4\kappa t)} - e^{-(z+z')^2/(4\kappa t)} \right] dz', \quad (4)$$

where z' is a dummy variable. Hence, we first let:

$$v = T - T_{atm}. \quad (5)$$

Then the boundary condition for v becomes:

$$v|_{z=0} = 0, \quad (6)$$

and the initial condition for v becomes:

$$v|_{t=0} = \phi(z) = \begin{cases} T_p - T_{atm} & 0 < z < z_1 \\ T_f - T_{atm} & z_1 < z < z_2 \\ T_g - T_{atm} & z > z_2 \end{cases} \quad (7)$$

The solution for v is therefore:

$$\begin{aligned} v(z, t) &= \frac{1}{\sqrt{4\pi\kappa t}} \int_0^{\infty} \phi(z') \cdot \left[e^{-(z-z')^2/(4\kappa t)} - e^{-(z+z')^2/(4\kappa t)} \right] dz' \\ &= \frac{1}{\sqrt{4\pi\kappa t}} \int_0^{z_1} (T_p - T_{atm}) \cdot \left[e^{-(z-z')^2/(4\kappa t)} - e^{-(z+z')^2/(4\kappa t)} \right] dz' \\ &\quad + \frac{1}{\sqrt{4\pi\kappa t}} \int_{z_1}^{z_2} (T_f - T_{atm}) \cdot \left[e^{-(z-z')^2/(4\kappa t)} - e^{-(z+z')^2/(4\kappa t)} \right] dz' \\ &\quad + \frac{1}{\sqrt{4\pi\kappa t}} \int_{z_2}^{\infty} (T_g - T_{atm}) \cdot \left[e^{-(z-z')^2/(4\kappa t)} - e^{-(z+z')^2/(4\kappa t)} \right] dz'. \end{aligned} \quad (8)$$

where z' is a dummy variable. Carrying out the integration and recognizing that $T=v+T_{atm}$, we obtain:

$$\begin{aligned} T(z, t) &= T_{atm} + \frac{T_p - T_{atm}}{2} \cdot \left[\operatorname{erf} \frac{z_1 - z}{\sqrt{4\kappa t}} + 2\operatorname{erf} \frac{z}{\sqrt{4\kappa t}} - \operatorname{erf} \frac{z_1 + z}{\sqrt{4\kappa t}} \right] \\ &\quad + \frac{T_f - T_{atm}}{2} \cdot \left[\operatorname{erf} \frac{z_2 - z}{\sqrt{4\kappa t}} - \operatorname{erf} \frac{z_1 - z}{\sqrt{4\kappa t}} + \operatorname{erf} \frac{z_1 + z}{\sqrt{4\kappa t}} - \operatorname{erf} \frac{z_2 + z}{\sqrt{4\kappa t}} \right] \\ &\quad + \frac{T_g - T_{atm}}{2} \left[\operatorname{erf} \frac{z_2 + z}{\sqrt{4\kappa t}} - \operatorname{erf} \frac{z_2 - z}{\sqrt{4\kappa t}} \right]. \end{aligned} \quad (9)$$

The cooling rate for a given position at a given time can be found by differentiating the above:

$$\begin{aligned} q(z, t) &= -\frac{dT}{dt} = \frac{T_p - T_{atm}}{\sqrt{16\pi\kappa t^3}} \cdot \left[(z_1 - z)e^{-(z_1-z)^2/(4\kappa t)} + 2ze^{-z^2/(4\kappa t)} - (z_1 + z)e^{-(z_1+z)^2/(4\kappa t)} \right] \\ &\quad + \frac{T_f - T_{atm}}{\sqrt{16\pi\kappa t^3}} \left[(z_2 - z)e^{-(z_2-z)^2/(4\kappa t)} \cdot (z_1 - z)e^{-(z_1-z)^2/(4\kappa t)} (z_1 + z)e^{-(z_1+z)^2/(4\kappa t)} \right. \\ &\quad \left. + - (z_2 + z)e^{-(z_2+z)^2/(4\kappa t)} \right] \\ &\quad + \frac{T_g - T_{atm}}{\sqrt{16\pi\kappa t^3}} \left[(z_2 + z)e^{-(z_2+z)^2/(4\kappa t)} - (z_2 - z)e^{-(z_2-z)^2/(4\kappa t)} \right]. \end{aligned} \quad (10)$$

The above solution can be easily implemented with a spreadsheet program. A copy of the program can be requested from one of the authors (Y.Z.).

When κ varies from layer to layer, a numerical, finite-volume solution is used (Fig. 9). The finite-volume method uses central differencing in space and was fully implicit in time yielding second-order accurate results (Patankar 1980; Versteeg and Malalasekera 1995). Grid points were generated every 0.01 m in the area of interest, and the calculation domain was extended to a sufficient depth so that conduction did not affect the bottom

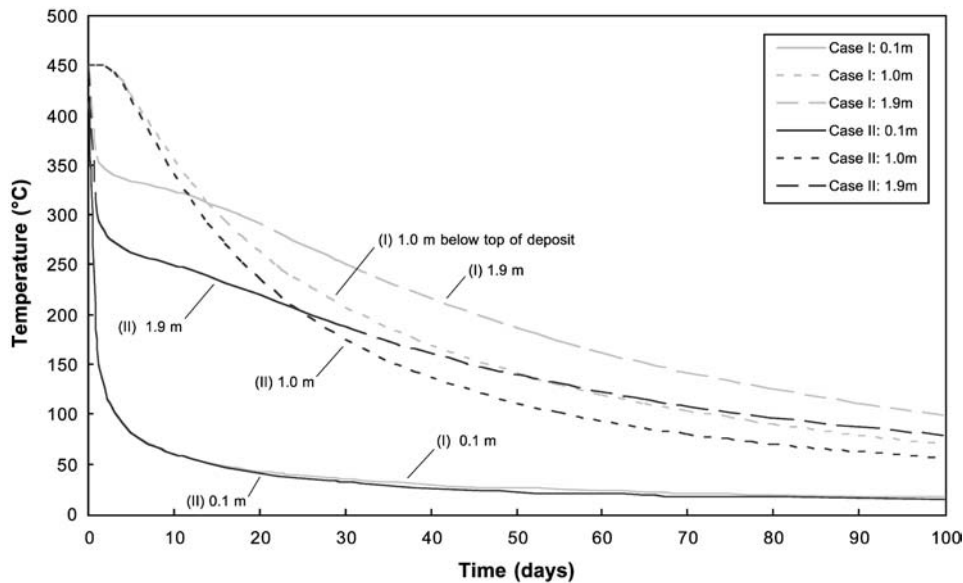


Fig. 11 Temperature vs. time for selected positions within a 2-m-thick pyroclastic-flow deposit. Values indicate the distance below the top of the deposit. Case *I* is for a numerical solution in which the flow deposit ($\kappa=0.003 \text{ cm}^2 \text{ s}^{-1}$) and underlying ground layer ($\kappa=0.015 \text{ cm}^2 \text{ s}^{-1}$) have different thermal diffusivities. Case *II* is for

an analytical solution with $\kappa=0.003 \text{ cm}^2 \text{ s}^{-1}$ for both layers. Note that although the flow is thin and initially only $450 \text{ }^\circ\text{C}$, it takes more than 10 days for its base to cool to $250 \text{ }^\circ\text{C}$. Estimates for the duration of formation of the Bishop Tuff (Anderson 1991; Wilson and Hildreth 1997) are less than this

boundary condition. The physical parameters were identical to those used in the analytical solution, except for the thermal diffusivity of the pre-eruptive basal (ground) layer. In the numerical simulations a basal, country-rock thermal diffusivity of $1.5 \times 10^{-6} \text{ m}^2 \text{ s}^{-1}$ ($0.015 \text{ cm}^2 \text{ s}^{-1}$) was used to test the sensitivity of the results to a more conductive material at the base than the overlying ignimbrite. The numerical scheme has been compared to the analytical solution for cases of constant κ across the layers, and the results are in agreement with a calculation uncertainty on the order of $0.001 \text{ }^\circ\text{C day}^{-1}$ ($10^{-8} \text{ }^\circ\text{C s}^{-1}$).

To test the analytical model, we calculated thermal profiles for a simple case in which a hot pyroclastic-flow deposit is emplaced directly on cold ground, and compared our profile to the in-situ temperature measurements of a Mount St. Helens pyroclastic-flow deposit (Ryan et al. 1990). Our analytical model fits the observed temperatures for thermal diffusivities that are close to those obtained by the Ryan et al. (1990) finite-difference model (Fig. 10a). Thus, for the purposes of this work we adopt a thermal diffusivity of $0.003 \text{ cm}^2 \text{ s}^{-1}$ for silicic pyroclastic deposits. We also tested the sensitivity of the thermal-conduction model by varying key parameters such as deposit thickness, emplacement temperature, and thermal diffusivity (Fig. 10b). The uncertainty in the thermal diffusivity is about $\pm 30\%$, resulting in temperature uncertainties in the thermal profile of $\pm 50 \text{ }^\circ\text{C}$.

As a conceptual aid, we first model the cooling history of a 2-m-thick pyroclastic-flow deposit emplaced at $450 \text{ }^\circ\text{C}$. We focus on the portion of the cooling history that would be recorded by hydrous speciation in rhyolitic glass. Then we model the effect of variations in thickness and emplacement temperature on theoretical cooling

rates. A pyroclastic-flow deposit cools from both above and below, and the conditions at the top and bottom boundaries largely govern the resulting cooling patterns. Positions near the top of the deposit are close to the flow-air interface where the temperature remains low and roughly constant. These positions, such as that at a depth of 0.1 m below the top of the deposit, cool very rapidly (Fig. 11). Positions near the base of the deposit (depth of 1.9 m) also cool rapidly initially but, as the subjacent ground warms, the cooling rate at a depth of 1.9 m decreases. The slowest cooling occurs initially near the middle of the deposit (1.0-m depth, Fig. 11), because it is the most insulated from the cool boundaries. With time the thermal maximum that is initially near the middle of the flow moves downwards and eventually conduction from the top governs cooling of even the basal layers. At the level of the thermal maximum the cooling rate is a minimum and, as this level passes downwards past a certain height, the cooling rate actually increases slightly before slowing again as the local temperature finally approaches the $10 \text{ }^\circ\text{C}$ temperature at the top of the deposit (view Fig. 11 obliquely and along the time axis to see the hump in the curve at 1.9-m depth).

The observed cooling rate reflected in a certain $\text{H}_2\text{O}_m\text{-OH}$ speciation in rhyolitic glass inclusions can be non-unique. In Fig. 12, for example, a cooling rate of about $5 \times 10^{-5} \text{ }^\circ\text{C s}^{-1}$ occurs three times: once at about 3 days, again at 12 days, and finally at about 30 days. As shown on Fig. 12, the cooling rate near the base (1.9-m depth) reaches a local minimum about 7 days after deposition. This is when the thermal maximum (where the temperature gradient is zero) reaches that specific level. Then the cooling rate increases as the thermal maximum passes

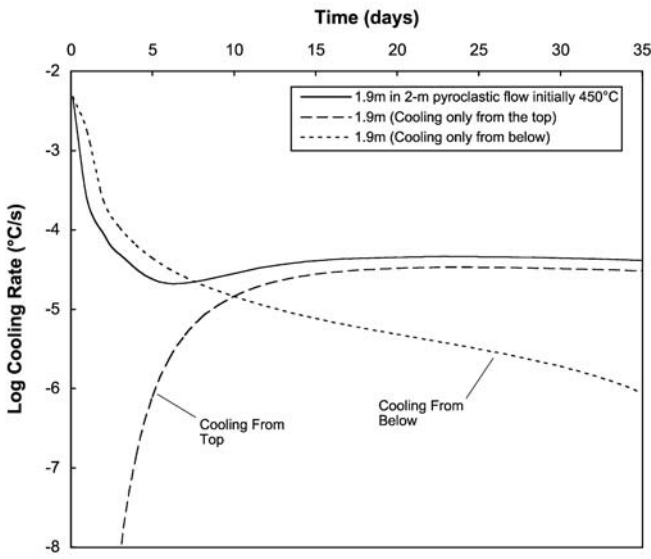


Fig. 12 Cooling rate versus time near the base (1.9-m depth in deposit) of a 2-m-thick pyroclastic-flow deposit. The separate effects of heat loss only through the top and base of the deposit are shown as *dashed lines*

downwards and the position is on the steeper, negative temperature gradient towards the top. The negative temperature gradient at the specified position (1.9-m depth, Fig. 12) eventually decreases and so does the cooling rate. Note that temperature declines continuously so that each time the cooling rate attains $5 \times 10^{-5} \text{ }^\circ\text{C s}^{-1}$ it does so at successively lower temperatures. Because the calculated cooling rate from a specific IR spectrum is at a specific temperature (T_{ae}), when the model is compared with observations, using both the temperature and the cooling rate removes the ambiguity. The overall pattern of cooling at a point near the flow base can thus be an early decrease in the rate of cooling, then a slight increase in the rate of cooling (as the spatial temperature maximum passes downwards past the point in the flow), and finally a decreasing rate of cooling to a stable, constant-temperature condition. This complex pattern of cooling will occur only for a limited range of levels in the flow.

Interpretation of hydrous speciation in rhyolitic glass

The final hydrous speciation of glass inclusions within a pyroclastic-flow deposit will be established at different times at different levels. Figure 13 helps reveal the aspects of cooling that the speciation records by showing cooling rates plotted against temperature. Cooling curves for 0.1-, 1.0- and 1.9-m depths and certain times in days are indicated on the respective curves. Figure 13 shows also the experimentally determined relationship between cooling rate and T_{ae} for given total H_2O contents. Hydroxyl and molecular water species remain in equilibrium along the portion of each model cooling curve (near-vertical curves) that lies above the experimental cooling

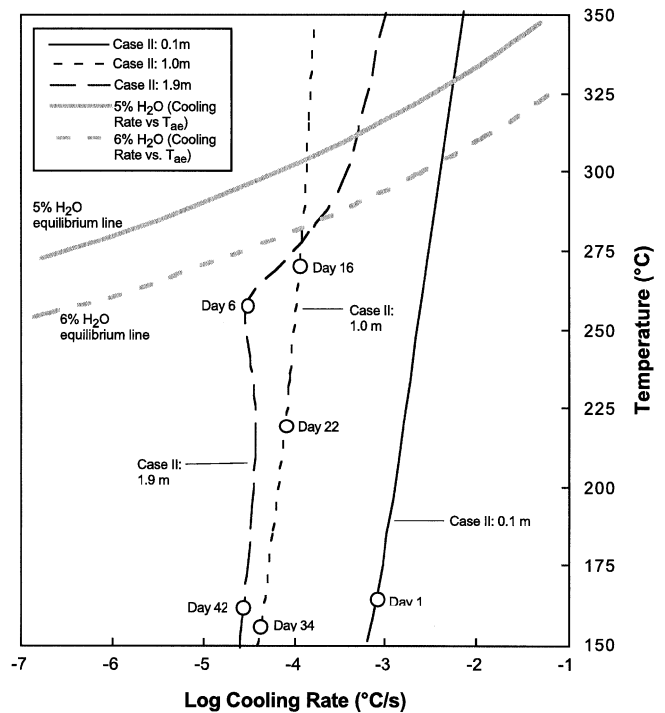


Fig. 13 Modeled cooling rate versus temperature for selected positions in a 2-m-thick pyroclastic-flow deposit. Values indicate the distance below the top of the deposit. Various times in days after emplacement are noted along the curves. Cooling-rate curves are calculated using an analytical heat-conduction solution with $\kappa=0.003 \text{ cm}^2 \text{ s}^{-1}$ for both layers (case II of Fig. 11). Also shown are the *lines* of apparent temperature of equilibrium (T_{ae}) with their corresponding predicted cooling rates for 5 and 6 wt% total water content (Zhang et al. 2000). The intersection of the modeled cooling-rate curves with the experimental cooling rate versus T_{ae} curves marks the condition where hydrous speciation is recorded in the inclusion. Propagation of a $\pm 30\%$ uncertainty in the thermal diffusivity leads to uncertainties of approximately 30% in the theoretical cooling rates. In applying this model to cooling rates of natural inclusions, uncertainties in H_2O content will typically lead to uncertainties of about 0.1 log unit in predicted cooling rate. However, for situations like the curve for case II, 1.9 m, the uncertainty could be as large as ± 0.3 log units

rate vs. T_{ae} lines (diagonal shaded curves). Note that faster cooling causes the model cooling curves to intersect the experimental cooling rate vs. T_{ae} lines at higher temperature. Approximately when the pyroclastic-flow deposit cooling-rate curves intersect the experimental lines, the final speciation will be locked into rhyolitic glass inclusions and thus record the implied cooling rates and T_{ae} values. This locking-in of the hydrous speciation will occur at different times for the different levels in the deposit.

Figure 13 illustrates also the dependence of T_{ae} and apparent cooling rate recorded by hydrous speciation on the total H_2O content. For higher water contents, lower cooling rates will be recorded, although the magnitude of this effect depends on the slope of the model cooling curves. In the basal region (1.9-m depth) the theoretical cooling curve may intersect the experimental cooling rate vs. T_{ae} line (diagonal shaded curve) where the theoretical

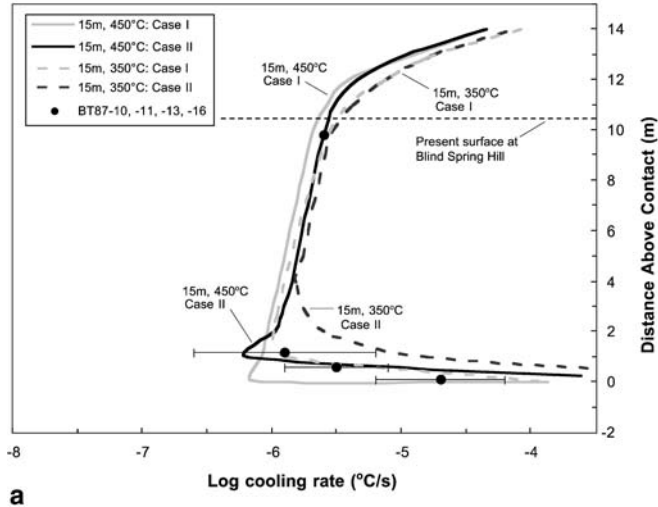


Fig. 14a, b Comparison of theoretical cooling rates at the apparent temperature of equilibrium (T_{ae}) and observed cooling rates from hydrous speciation in glass inclusions. Curves show cooling rates predicted to be recorded by glass inclusions in **a** 15- and **b** 50-m-thick pyroclastic flow deposits with various initial temperatures calculated using case I and case II described in Fig. 11. The theoretical curves for the 15-m-thick deposits are calculated for inclusions with 6 wt% H_2O whereas the curves for the 50-m-thick deposits are for inclusions with 4 wt% H_2O . These values were chosen so the curves could be compared most directly with the Blind Spring Hill (inclusions have ~6 wt% H_2O) and Crestview (inclusions have ~4 wt% H_2O) data. Each point on a given cooling-rate curve was generated in the same manner as in Fig. 13, that is, the cooling rate for hydrous glass at a particular depth in the deposit is 'locked in' when the theoretical cooling curve (vertical lines in

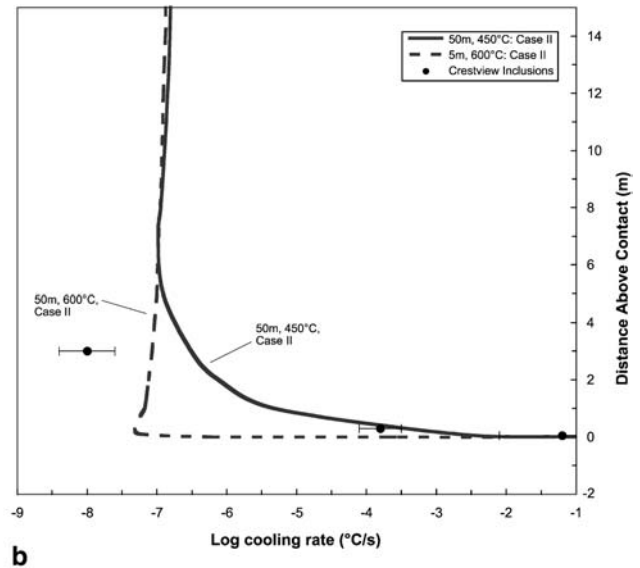


Fig. 13) intersects the appropriate experimental cooling-rate versus T_{ae} curve (shaded curves in Fig. 13). Data points are shown for inclusion averages for pyroclastic-flow deposits shown in Figs. 6, 7, and 8. Note that the theoretical cooling-rate curves are somewhat sensitive to the H_2O content of the glass: glass with 6 wt% (e.g., F7 at Blind Spring Hill) as compared with 4 wt% H_2O (Ig2NWa at Crestview) is predicted to record a slower cooling rate by about a factor of 10 to 100. Thus, if we had displayed the cooling rates for a 50-m-thick pyroclastic flow based on 6 rather than 4 wt% H_2O in the glass, then the curves for the 50-m-thick flows would be shifted to even slower cooling rates, farther away from the cooling rates for the 15-m-thick flow with 6 wt% H_2O inclusion glasses. The comparatively smaller cooling rates for the hypothetical 50-m-thick flows thus primarily reflect their greater thickness

cooling-rate curve fluctuates in response to a switch over from cooling to the base to cooling to the top.

Comparison between observed and modeled cooling rates can help constrain original pyroclastic-flow emplacement temperature and thickness. We combined our model of conductive cooling together with the Zhang et al. (2000) experimental cooling curves (for example, as shown on Fig. 13) to predict cooling rates that we would expect to be recorded by the hydrous speciation in rhyolitic glass inclusions.

Our model results are calculated for hypothetical 15-m-thick pyroclastic-flow deposits with initial temperatures of 350 and 450 °C (Fig. 14a), and for 50-m-thick deposits with initial temperatures of 450 and 600 °C (Fig. 14b). Examination of the profiles for the two 15-m-thick deposits reveals the somewhat counter-intuitive result that a higher emplacement temperature yields lower theoretical cooling rates in the basal part of the pyroclastic flow. The 350 °C flows are cool enough initially such that their base cools through the hydrous-species equilibrium curve relatively early in the cooling history. Hence, the speciation near its base records the fast initial cooling of the layer in contact with the cool ground. The 450 °C flow cools for a much longer period of time before reaching about 300 °C where final speciation is recorded.

Due to the longer time to cool to around 300 °C, the cooling of the basal region at the time speciation is recorded reflects cooling to the top of the pyroclastic flow. Thus, the hydrous speciation in the 350 °C flow base is quenched during initial, rapid cooling to the underlying ground. By contrast, the hydrous speciation in the basal part of the 450 °C flow is recorded only while slowly cooling to the top through the overlying pyroclastic-flow blanket.

Figure 14b shows the expected theoretical result that a 50-m-thick pyroclastic-flow deposit would have hydrous speciations that record much slower rates of cooling, regardless of the original temperature of the flow. There are no conditions whereby a 15-m-thick deposit is predicted to quench in cooling rates as low as $10^{-8} \text{ °C s}^{-1}$, which are attained within the lower 3 m of the 50-m-thick deposit. In this way cooling rates can constrain the initial thickness of a pyroclastic-flow deposit.

The initial temperature, on the other hand, can be constrained from the vertical position at which the minimum recorded cooling rate occurs. For a 600 °C, 50-m-thick deposit, the minimum cooling rate of about $6 \times 10^{-8} \text{ °C s}^{-1}$ occurs at about 0.1 m above the base, and this moves up to about 7 m and $10^{-7} \text{ °C s}^{-1}$ for a 450 °C, 50-m-thick deposit (Fig. 14b). Thus, given observed

cooling rates through the lower 3 to 10 m of a pyroclastic-flow deposit, it is possible to constrain both its initial emplacement temperature and thickness.

Cooling rates of Plinian-fall deposits

The cooling rates of the most rapidly cooled, Plinian Bishop glass inclusions (within 2 m of the base of the Blind Spring Hill pumice-fall deposit) are shown in Fig. 15. Shown for comparison are conductive-cooling rates for the interiors of pumice clasts falling through cold air calculated by Tait et al. (1998). The calculated conductive-cooling rates are minima because they are for the clast center; the average cooling rate for the entire clast would be greater because the outer portions of a clast cool faster (e.g., Hort and Gardner 2000). The Bishop glass inclusions come from pumice clasts <4 cm in diameter, and the cooling rates derived from hydrous-speciation data agree well with theoretical conductive-cooling rates.

It is of interest to compare the cooling rates of bubble-free and bubble-bearing glass inclusions, because a bubble-free inclusion will pull on the quartz wall with cooling (differential thermal contraction) and the glass will be under a tensile stress. The bubble relieves this stress. Cooling rates of bubble-free and bubble-bearing glass inclusions from a given sample are indistinguishable, and this shows that the tensile stress in bubble-free glass inclusions has negligible effect on either the equilibrium speciation or the infrared spectra.

We also show in Fig. 15 calculated cooling rates for rhyolitic obsidian clasts (mostly <1 cm diameter) from air-fall tephra at Mono Craters, California (Newman et al. 1988). These dense obsidians contain <3 wt% total water, compared to ~4 to 6 wt% total H₂O in the Bishop glass inclusions, yet the cooling rates based on water speciation are similar for the separate sets of samples, in agreement with their similar eruptive and depositional histories. This similarity and the agreement with the theoretical conductive-cooling estimates suggests that rhyolitic glass inclusions in Plinian tephra are accurate recorders of cooling rates during eruptive dispersal.

Cooling rates of pyroclastic-flow deposits

Observed cooling rates for Bishop glass inclusions from pyroclastic-flow deposits suggest cooling rates of $\sim 10^{-6}$ to 10^{-8} °C s⁻¹. However, in the lowermost regions of these deposits, where they are chilled against cold ground or underlying Plinian-fall deposits, cooling rates as high as 10^{-1} °C s⁻¹ are observed. Cooling rates for thick, partially welded portions of the Bishop Tuff outflow sheet have been estimated at 10^{-7} to 10^{-8} °C s⁻¹ based on the kinetics of oxygen isotopic exchange of feldspar phenocrysts with hydrothermal fluids (Holt and Taylor 1998). Although these rates are similar to our results based on hydrous speciation in glass inclusions, a direct comparison is

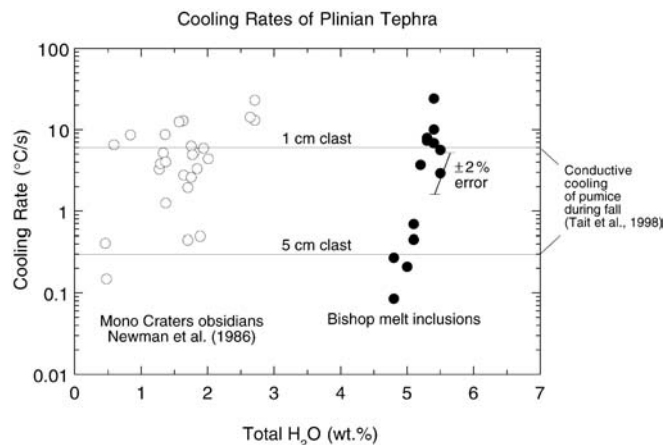


Fig. 15 Cooling rate versus total H₂O concentration. Data for Bishop Plinian-fall glass inclusions are from clasts BT87-2, -3, and -5. Data are from Table 2. Error bar shows the effect of $\pm 2\%$ uncertainty in measuring the thickness of glass inclusions. Because the sample thickness affects both the total H₂O and the cooling rate determined from IR data, uncertainties cause a positive correlation on this diagram. Water speciation data for Mono Craters obsidians are from Newman et al. (1986), and cooling rates for these samples are calculated from Zhang et al. (2000), so they are directly comparable to rates calculated for the Bishop glass inclusions. Conductive-cooling rates for spherical pumice clasts falling through cold air are from Tait et al. (1998)

difficult because of the differences between their samples and ours, which come from relatively thin, non-welded and non-hydrothermally altered flow deposits.

The data for the Crestview inclusions (~4 wt% H₂O) are plotted on Fig. 14b and they fall within error of the theoretical curves for a 50-m-thick deposit, except for the samples at 3.0 m whose extrapolated cooling rate is slightly lower than predicted values. This is consistent with the geological constraints for a minimum thickness of about 30 m at this locality (Hildreth, oral communication 1999). Observed cooling rates for inclusions in the pyroclastic-flow deposit at Blind Spring Hill fall within uncertainty of the theoretical cooling curves for 15-m-thick flow deposits (Fig. 14a), consistent with the evidence summarized above for an initial thickness <17 m. At Chalfant Quarry and Chalk Bluffs, our limited sampling does not provide much constraint on either flow-deposit thickness or initial temperature. However, geologic evidence suggests initial Ig2 thicknesses possibly >50 m at Chalfant and >100 m at Chalk Bluffs (Wilson and Hildreth 1997). The range of observed cooling rates for Chalk Bluffs glass inclusions is consistent with their location in the rapidly cooled, basal region of thick pyroclastic-flow deposits (see Fig. 14b). At Chalfant, we note that uncracked glass inclusions remain glassy only within about 1.5 m of the base of the Ig2Ea pyroclastic flow; above this level, inclusions are devitrified.

It has been inferred from data on sanidine cryptocrystals in the thick, welded ignimbrite southeast of Long Valley Caldera that emplacement of the Gorges and

Tableland lobes of the Bishop Tuff were separated by several years (Snow and Yund 1988). This contrasts with volcanological observations that show no evidence of such a time break, and from which it has been inferred that emplacement of the entire Bishop Tuff occurred during a single eruption with a duration of about 4 days (Wilson and Hildreth 1997). We have not sampled the thick, welded ignimbrite from which the cryptoperthite data are derived because our experience shows that glass inclusions from such slowly cooled deposits would undoubtedly be crystallized. Thus, our data and modeling do not provide any evidence either for or against the time break inferred from the feldspar data. We note, however, that in non-welded deposits the glass-inclusion, H₂O geospeedometer could resolve such time breaks only if there was a sufficient gap of time so that the underlying deposits had cooled significantly. This would cause rapid quenching of glass inclusions at the base of the overlying deposit, similar to our results for the lowermost deposits at the Crestview locality (Fig. 8).

Resetting of hydrous speciation in Plinian deposits by overlying pyroclastic flows

We used our model to evaluate possible resetting of cooling rates of Plinian inclusions caused by an overlying, hot pyroclastic flow (Fig. 9). The modeled temperature of the Plinian deposit first rises, with strata nearer to the contact heating faster and to a greater temperature than lower strata. The amount of reheating increases with the temperature and thickness of the overlying, hot pyroclastic-flow deposit. Modeled cooling of the reheated Plinian strata is depicted in Fig. 16. A 15-m-thick pyroclastic-flow deposit emplaced at 450 °C does not sufficiently reheat the underlying Plinian deposit 0.1 m below the contact to reset the hydrous speciation. A deposit 15 m thick, if emplaced at 600 °C, would reheat the Plinian deposits 1.0 m below the contact to a high enough temperature to potentially reset the speciation for 6 wt% total H₂O. However, the cooling rates for this case increase very rapidly (resulting in the subhorizontal cooling trajectories on Fig. 16 as the thermal maximum moves downwards). As a result the glass would spend very little time cooling slowly. Therefore, the speciation probably would not relax to the appropriate value. Closer to the Plinian/pyroclastic-flow boundary (0.1 m below contact), however, the cooling rate is approximately constant as it intersects the 6% water speciation curve, and resetting of the Plinian deposits is expected. Thus, reset speciations also can constrain the initial characteristics of the overlying pyroclastic-flow deposit.

Cooling rates of Plinian inclusions were reset in the upper part of the Plinian deposit at both Blind Spring Hill and Chalfant (Figs. 6, 7). In the case of Blind Spring Hill, the cooling rate of Plinian inclusions decreases upwards to about 10⁻³ °C s⁻¹ at ~4 m above the base of the Plinian deposit. Our sampling of Chalfant Plinian deposits is more limited but Plinian inclusions less than 1 m below

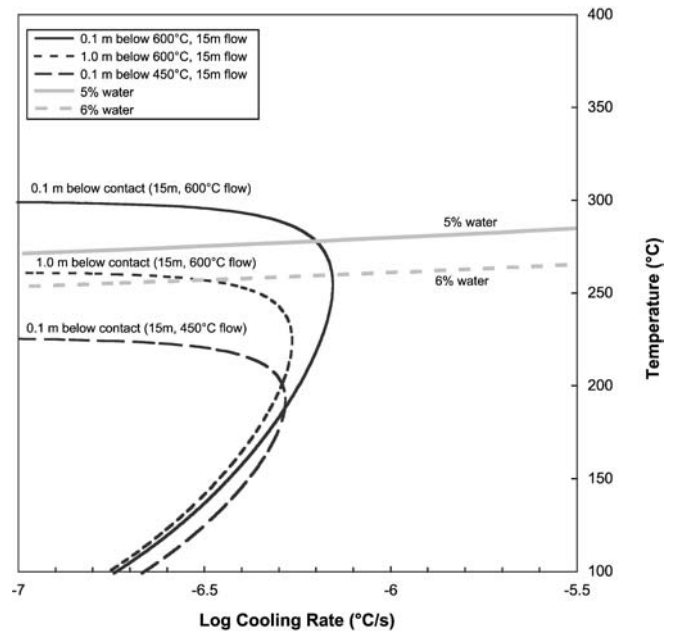


Fig. 16 Cooling rate versus temperature of Plinian-fall deposits buried underneath subsequent hot pyroclastic-flow deposits. Values indicate the distance below the contact between the overlying pyroclastic-flow deposit and underlying Plinian-fall deposit (see text for description of model)

the pyroclastic-flow deposit show cooling rates of 10⁻⁴ to 10⁻⁷ °C s⁻¹. In both cases, the evident resetting of the observed cooling rates of Plinian inclusions a meter or so below the overlying pyroclastic-flow deposits suggests that initial temperature of the flow deposit was >450 °C (Fig. 16).

Conditions necessary for preservation of bubble-free, glassy melt inclusions

Melt inclusions are glassy and mostly bubble-free in distal Bishop Plinian-fall deposits (Fig. 3a, b). In proximal counterparts, such as the 25-cm-thick stratum between two pyroclastic flows on the shore of Lake Crowley (locality 2 of Wilson and Hildreth 1997), uncracked glass inclusions are devitrified. Uncracked glass inclusions are glassy in the Plinian deposit exposed in the Highway 397 roadcut at Sherwin Grade (Figs. 2, 7) but most contain bubbles. In pyroclastic-flow deposits that are non-welded, there is a wide range of glass-inclusion textures that vary from glassy and slightly colored (Fig. 3c) to slightly devitrified (finely speckled; Fig. 3e, g, k) and devitrified (crystals 1–10 µm in size; Fig. 3f, j, l). Some inclusions from basal pyroclastic flows contain a few ~10 µm crystals that are attached to the inclusion wall (Fig. 3g, h, l) and these may have attached bubbles (Fig. 3g, l). The size, number density and distribution of bubbles in reentrants and hourglass inclusions (Fig. 3m) vary mainly with hourglass shapes (which control their degassing; Anderson 1991) but also correlate somewhat with stratum

(cooling rate). The extent of coloration or devitrification is typically similar for inclusions from a given stratum, and in some cases, such as the Crestview section, the extent of devitrification increases systematically upwards. In pyroclastic-flow deposits that are welded, glass inclusions are invariably crystallized.

We infer that preservation of bubble-free glassy inclusions reflects rapid cooling (plausibly greater than $0.001\text{ }^{\circ}\text{C s}^{-1}$) at temperatures above those at which the hydrous speciation is recorded ($>400\text{ }^{\circ}\text{C}$). With slower cooling at $T > 400\text{ }^{\circ}\text{C}$, inclusions nucleate and grow bubbles; with even slower high-temperature cooling, devitrification occurs. Although devitrification and bubble formation are sensitive to H_2O , the temperature vs. cooling-rate space over which bubbles and crystals formed in the Bishop Tuff is quite limited. These observations have implications for natural rates of nucleation and growth of bubbles and crystals as well as for sampling strategies aimed at glassy melt inclusions. Melt inclusions in pyroclastic-flow deposits appear to be quenched to glass only if the deposit is relatively thin or has a relatively low emplacement temperature. Our work shows that in relatively thick or hot deposits, inclusions may be preserved to glass at the base of the deposit where it is more rapidly cooled by contact with the pre-eruption ground.

Conclusions

Cooling rates inferred from water speciation in glass inclusions are consistent with theoretical expectations for Plinian-fall tephra ($1\text{ to }10\text{ }^{\circ}\text{C s}^{-1}$) and for pumice from $>2\text{ m}$ above the base in pyroclastic flows ($10^{-6}\text{ to }10^{-8}\text{ }^{\circ}\text{C s}^{-1}$). The observed cooling rates appear to be as accurate as they are precise, notwithstanding the fact that natural cooling rates change with cooling, whereas the experimental calibrations of Zhang et al. (2000) are based on constant rates of cooling and are extrapolated to cooling rates slower than $0.0001\text{ }^{\circ}\text{C s}^{-1}$. Hydrous speciation and inferred cooling rates of glass inclusions are quenched in (recorded) at temperatures ranging from about $\sim 400\text{ }^{\circ}\text{C}$ ($1\text{ to }10\text{ }^{\circ}\text{C s}^{-1}$) to $\sim 250\text{ }^{\circ}\text{C}$ ($10^{-8}\text{ }^{\circ}\text{C s}^{-1}$).

Our thermal modeling reveals that the cooling history within and below a pyroclastic flow can be surprisingly complex. For example, hotter pyroclastic flows will generally record slower cooling rates in their basal strata. Also, a stratum can cool at a specified rate at different times and temperatures. Observed cooling rates for inclusions from the lower 3 m of a pyroclastic-flow deposit can constrain both its initial T and its thickness. For example, at the Blind Spring Hill locality where a pyroclastic-flow deposit $\sim 15\text{ m}$ thick overlies a Plinian deposit, the reset cooling rates of glass inclusions in Plinian pumice and the cooling rates of glass inclusions in the pyroclastic-flow deposit reveal that the pyroclastic-flow deposit was hotter than $450\text{ }^{\circ}\text{C}$ (otherwise it would not reset the Plinian glass inclusions) and thinner than

50 m (otherwise the pyroclastic-flow inclusions would have cooled more slowly than observed).

Future applications of the water-speciation cooling-rate speedometer have the potential, by using a dedicated sampling strategy, to provide detailed information on deposition temperatures of pyroclastic-flow deposits, and thus on cooling of pyroclastic flows with distance from source. Cooling rates may also constrain the original thickness of pyroclastic deposits, which could be used along with the age of the deposit to provide a measure of erosion rate. Finally, anomalous cooling rates may reveal the presence of snowpacks beneath certain deposits, and this could reveal seasonal and climatic factors.

Acknowledgements It is a pleasure to record our thanks to Colin Wilson and Wes Hildreth for guidance in the field and for discussions, and to Yang Liu for help with spectral analyses of some inclusions. We also thank Doug MacAyeal, Richard Wardle and George Bergantz for discussions regarding thermal modeling, and Jim Gardner, Sally Newman, and Tim Druitt for helpful reviews that led to significant improvements in the final manuscript. The work was supported in large part by NSF grants EAR 9706330 and 0001154.

References

- Anderson AT Jr (1991) Hourglass inclusions: theory and application to the Bishop rhyolitic tuff. *Am Mineral* 76:530–547
- Anderson AT Jr, Newman S, Williams SN, Druitt TH, Skirius C, Stolper E (1989) H_2O , CO_2 , Cl, and gas in Plinian and pyroclastic-flow Bishop rhyolite. *Geology* 17:221–225
- Anderson AT Jr, Davis AM, Lu F (2000) Evolution of Bishop Tuff rhyolitic magma based on melt and magnetite inclusions, and zoned phenocrysts. *J Petrol* 41:449–473
- Bailey RA, Dalrymple GB, Lanphere MA (1976) Volcanism, structure and geochronology of Long Valley Caldera, Mono County, California. *J Geophys Res* 81:725–744
- Carslaw HS, Jaeger JC (1959) Conduction of heat in solids. Oxford University Press, Oxford
- Dunbar NW, Hervig RL (1992) Petrogenesis and volatile stratigraphy of the Bishop Tuff: evidence from melt inclusion analysis. *J Geophys Res* 97:15129–15150
- Hildreth W, Mahood GA (1986) Ring-fracture eruption of the Bishop Tuff. *Geol Soc Am Bull* 97:396–403
- Holt EW, Taylor HP, Jr (1998) $^{18}\text{O}/^{16}\text{O}$ mapping and hydrogeology of a short-lived (~ 10 years) fumarolic ($>500\text{ }^{\circ}\text{C}$) meteoric-hydrothermal event in the upper part of the 0.76 Ma Bishop Tuff outflow sheet, California. *J Volcanol Geotherm Res* 83:115–139
- Hort M, Gardner J (2000) Constraints on cooling and degassing of pumice during Plinian volcanic eruptions based on model calculations. *J Geophys Res* 105:25981–26001
- Ihinger PD, Zhang Y, Stolper EM (1999) The speciation of dissolved water in rhyolitic melt. *Geochim Cosmochim Acta* 63:3567–3578
- Lu F (1991) The Bishop Tuff: origins of the high-silica rhyolite and its thermal and chemical zonations. PhD Thesis, University of Chicago
- Newman S, Stolper EM, Epstein S (1986) Measurement of water in rhyolitic glasses: calibration of an infrared spectroscopic technique. *Am Mineral* 71:1527–1541
- Newman S, Epstein S, Stolper E (1988) Water, carbon dioxide, and hydrogen isotopes in glasses from the ca. 1340 A.D. eruption of the Mono Craters, California: constraints on degassing phenomena and initial volatile content. *J Volcanol Geotherm Res* 35:75–96

- Patankar SV (1980) Numerical heat transfer and fluid flow. Hemisphere Publ Corp, Taylor & Francis Group, New York
- Riehle JR (1973) Calculated compaction profiles of rhyolitic ash-flow tuffs. *Bull Geol Soc Am* 84:2193–2216
- Riehle JR, Miller TF, Bailey RA (1995) Cooling, degassing and compaction of rhyolitic pyroclastic-flow deposit tuffs: a computational model. *Contrib Mineral Petrol* 57:319–336
- Ryan MP, Banks NG, Hoblitt RP, Blevins JYK (1990) The in-situ thermal transport properties and the thermal structure of Mount St. Helens eruptive units. In: Ryan MP (ed) *Magma transport and storage*. Wiley, New York, pp 137–155
- Silver LA, Ihinger PD, Stolper EM (1990) The influence of bulk composition on the speciation of water in silicate glasses. *Contrib Mineral Petrol* 14:142–162
- Skirius CM (1990) Preeruptive H₂O and CO₂ content of the Plinian and pyroclastic-flow Bishop Tuff magma. PhD Thesis, University of Chicago
- Skirius CM, Peterson JW, Anderson AT Jr (1990) Homogenizing rhyolitic glass inclusions from the Bishop Tuff. *Am Mineral* 75:1381–1398
- Smith RL (1960) Ash flows. *Bull Geol Soc Am* 71:795–842
- Snow E, Yund RA (1988) Origin of cryptoperthites in the Bishop Tuff and their bearing in its thermal history. *J Geophys Res* 93:8975–8984
- Sparks RSJ, Wright JV (1979) Welded airfall tuffs. *Geol Soc Am Spec Pap* 180:155–165
- Sparks RSJ, Tait SR, Yanev Y (1999) Dense welding caused by volatile resorption. *J Geol Soc Lond* 156:217–225
- Tait S, Thomas R, Gardner J, Jaupart C (1998) Constraints on cooling rates and permeabilities of pumice in an explosive eruption jet from colour and magnetic mineralogy. *J Volcanol Geotherm Res* 86:79–91
- Thomas RME, Sparks RSJ (1992) Cooling of tephra during fallout from eruption columns. *Bull Volcanol* 54:542–553
- van den Bogaard P, Schirnick C (1995) ⁴⁰Ar/³⁹Ar laser probe ages of Bishop Tuff quartz phenocrysts substantiate long-lived silicic magma chamber at Long Valley, United States. *Geology* 23:759–762
- Versteeg HK, Malalasekera W (1995) An introduction to computational fluid dynamics: the finite volume method. Prentice Hall, Pearson Education, London
- Wallace P, Anderson AT, Davis AM (1999) Gradients in H₂O, CO₂ and exsolved gas in a large-volume silicic magma system: interpreting the record preserved in melt inclusions from the Bishop Tuff. *J Geophys Res* 104:20097–20122
- Wilson CJN, Hildreth W (1997) The Bishop Tuff: new insights from eruptive stratigraphy. *J Geol* 105:407–439
- Xu Z, Zhang Y (2002) Quench rates in water, air and liquid nitrogen, and inference of temperature in volcanic eruption columns. *Earth Planet Sci Lett* 200:315–330
- Zhang Y, Stolper EM, Ihinger PD (1995) Kinetics of reaction H₂O + O = 2OH in rhyolitic glasses: preliminary results. *Am Mineral* 80:593–612
- Zhang Y, Jenkins J, Xu Z (1997a) Kinetics of the reaction H₂O + O = 2OH in rhyolitic glasses upon cooling: geospeedometry and comparison with glass transition. *Geochim Cosmochim Acta* 61:2167–2173
- Zhang Y, Belcher R, Ihinger PD, Wang L, Xu Z, Newman S (1997b) New calibration of infrared measurement of dissolved water in rhyolitic glasses. *Geochim Cosmochim Acta* 61:3089–3100
- Zhang Y, Zhengjiu X, Behrens H (2000) Hydrous species geospeedometer in rhyolite: improved calibration and application. *Geochim Cosmochim Acta* 64:3347–3355